Stress evolution in restrained GGBFS concrete due to autogenous deformation bayesian optimization of aging creep

Liang, Minfei; Li, Zhenming; He, Shan; Chang, Ze; Gan, Yidong; Schlangen, Erik; Šavija, Branko

DOI
10.1016/j.conbuildmat.2022.126690

Publication date
2022

Document Version
Final published version

Published in
Construction and Building Materials

Construction and Building Materials 324 (2022) 126690

Contents lists available at ScienceDirect

Construction and Building Materials

journal homepage: www.elsevier.com/locate/conbuildmat

Stress evolution in restrained GGBFS concrete due to autogenous deformation: bayesian optimization of aging creep

Minfei Liang, Zhenming Li, Shan He, Ze Chang *, Yidong Gan, Erik Schlangen, Branko Šavija

Microlab, Faculty of Civil Engineering and Geosciences, Delft University of Technology, Delft 2628, CN, the Netherlands

ARTICLE INFO

Keywords:
Concrete
Early age cracking
Creep
Relaxation
Autogenous shrinkage

ABSTRACT

Stress evolution of restrained concrete is a significant direct index in early-age cracking (EAC) analysis of concrete. This study presents experiments and numerical modelling of the early-age stress evolution of Ground granulated blast furnace slag (GGBFS) concrete, considering the development of autogenous deformation and creep. Temperature Stress Testing Machine (TSTM) tests were conducted to obtain the autogenous deformation and stress evolution of restrained GGBFS concrete. By a self-defined material subroutine based on the Rate-type creep law, the FEM model for simulating the stress evolution in TSTM tests was established. By characterizing the creep compliance function with a 13-units continuous Kelvin chain, forward modelling was firstly conducted to predict the stress development. Then inverse modelling was conducted by Bayesian Optimization to efficiently modify the arbitrary assumption of the codes on the aging creep. The major findings of this study are as follows: 1) the high autogenous expansion of GGBFS induces compressive stress at first hours, but its value is low because of high relaxation and low elastic modulus; 2) The codes highly underestimated the early-age creep of GGBFS concrete. They performed well in prediction of stress after 200 h, but showed significant gaps in predictions of early-age stress evolution; 3) The proposed inverse modelling method with Bayesian Optimization can efficiently adjusted the aging terms which produced best modelling results. The adjusted creep compliance function of GGBFS showed a much faster aging speed at early ages than the one proposed by original codes.

1. Introduction

Early-age cracking (EAC) is one of the trickiest problems in infrastructure constructions. EAC is the combined result of hydration reactions of cementitious materials and external actions. When the shrinkage of concrete structures is continuously restrained by boundary conditions, tensile stress will be gradually built up and cause EAC when it exceeds the tensile strength.

In view of the worldwide initiative of carbon reduction, recycling mineral materials are developed to replace Ordinary Portland Cement (OPC) as supplementary cementitious materials (SCMs). However, large incorporation of SCMs changes the hydration process of cementitious systems and therefore brings new problems in EAC analysis. Ground granulated blast furnace slag (GGBFS), one of the most popular SCMs retrieved from steel factories, has been extensively used in concrete structures. The replacement of OPC by GGBFS significantly reduces hydration heat and therefore effectively eases the threats of thermal shrinkage in EAC analysis. However, due to the lower elastic modulus and larger drop in relative humidity, GGBFS can lead to much higher autogenous shrinkage [12], which happens almost uniformly inside concrete and is likely to cause through cracks [3]. Shen et al [4] tested the stress of restrained GGBFS concrete induced by autogenous shrinkage and found a positive correlation between the content of GGBFS and EAC potential. They suggested that the replacement rate of OPC by GGBFS should not exceed 20% to prevent EAC. Except for the increasing risk of autogenous shrinkage, it was found that the autogenous deformation of GGBFS concrete started with expansion due to the creation of early-age hydrates [5]. Carette et al [6] observed an increasing swelling caused by GGBFS from the setting time to a degree of hydration close to 0.6, and attributed the high swelling to high amount of ettringite formation and low stiffness at early age. It is clear that the autogenous expansion of GGBFS concrete is in favor of preventing EAC, since it causes compressive stress under restraint conditions and delays the development of tensile stress. Therefore, to accurately quantify the EAC potential of GGBFS concrete, the autogenous expansion should not be neglected.

* Corresponding author.
E-mail addresses: M.Liang-1@tudelft.nl (M. Liang), Z.Li-2@tudelft.nl (Z. Li), S.He-2@tudelft.nl (S. He), Z.Chang-1@tudelft.nl (Z. Chang), Y.Gan@tudelft.nl (Y. Gan), Erik.Schlangen@tudelft.nl (E. Schlangen), B.Savija@tudelft.nl (B. Šavija).

https://doi.org/10.1016/j.conbuildmat.2022.126690
Received 23 November 2021; Received in revised form 23 January 2022; Accepted 29 January 2022
Available online 10 February 2022

Table 1
Mixes for TSTM tests (kg/m^3).

	CEM III B	Water	W/B	Sand (0–4 mm)	Gravel (4–16 mm)	Superplasticizer
Mix 1	320	160	0.50	811.8	1032	0
Mix 2		112	0.35			1.9

Table 2
CEM III/B 42.5 N characteristics.

Composition	wt. %	stdErr
CaO	47.11	0.140
SiO_2	29.11	0.370
Al_2O_3	10.02	0.180
MgO	5.89	0.140
SO_3	2.82	–
Fe_2O_3	1.19	0.030
TiO_2	0.82	0.012
K_2O	0.63	0.025
Na_2O	0.28	0.012
Mn_2O_3	0.20	0.010
P_2O_5	0.13	0.003

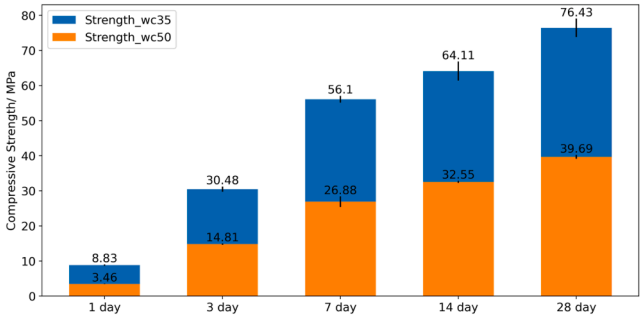

Fig. 1. Compressive strength of the two concrete mixes at different ages.

Another factor strongly influencing the stress build-up is creep/ relaxation, which should be taken into account in all cases of EAC analysis [78]. In the TSTM test conducted by Li et. al [9], the influence of stress relaxation was proved to be very significant in accurate estimation of stress evolvement. A number of studies [10-12] have confirmed that the double power law is an effective way to characterize the aging creep, which forms the basis for incorporating aging creep/ relaxation in EAC analysis. However, the early-age measurement of creep is often a problem because of difficulties in decoupling the hydration effects and creep strain measurement. Hassan et al [13] performed an hourly repeated minute-long test to measure the creep since the 21st hours after casting, and derived the aging creep data corresponding to different microstructures. Gao et al [14] performed the ring tests to measure the stress relaxation parameters of concrete in tension and fitted the results with power functions. Dabara et al [15] tested the tensile creep in early age and got the results that were much higher than Model Code 2010. Besides, many studies in EAC analysis often presumed the tensile and compressive creep/relaxation as the same [12]. However, Rossi et al [16] observed a greater difference between basic tensile and compressive creep in early age. The high magnitude and difference between tension and compression of creep measurement in early age emphasize the importance of early-age creep/ relaxation in EAC analysis. Another major challenge posed by creep/relaxation in EAC analysis is the incorporation of SCMs. Some studies [17,18] showed the SCMs could led to drastic increase of creep/ relaxation in early age due to slow hydration rates. Gan et al [19,20] performed micro-cantilever creep test by nano-indenter on OPC and GGBFS cement paste and compared the creep test results at micro- and macro- scale. Their results showed that 70% replacement of OPC by GGBFS promoted the magnitude of creep. However, there were also studies [21] observing lower creep of SCM concrete, which was attributed to the role of SCMs as fine aggregates. These contradictory findings pose difficulties for incorporating aging creep in EAC analysis.

To directly quantify the potential of EAC, a number of restraint testing methods have been developed, including rigid cracking frame test [22], internal restraint test by embedded reinforcement [23], ring test [24], and temperature-stress testing machine (TSTM) test [25,26]. Among all the testing methods, TSTM test stands out with the advantages of temperature control, flexible loading schemes and tunable restraint degrees, which can exclude the influence of thermal stress and allow both displacement-controlled test and load-controlled test [27]. Shen et al [4,25] performed TSTM tests on concrete with different amounts of GGBFS and temperature profiles and represented the cracking potential with stress/ strength ratio. Similarly, Markandeya et al [26] conducted TSTM tests on GGBFS concrete with different temperature profiles and found that high early-age reactivity (indicated by low MgO/Al_2O_3 ratio) of GGBFS significantly promote the cracking potential, which increases both heat release and autogenous shrinkage. Bouasker et al [28] conducted the ring tests to measure the stress development of binary and ternary cementitious materials and concluded that both limestone filler and GGBFS increase the magnitude of autogenous shrinkage but show later EAC compared with OPC concrete. With emphasis on realistic curing temperature regimes, Klausen et al [29] developed a EAC design methodology based on TSTM tests and analytical models. Their results show that TSTM tests have good reproducibility and are useful for characterization of material properties.

To summarize, current literatures on autogenous deformation, creep and TSTM test together established a comprehensive understanding on EAC. However, most studies gave hints on EAC of GGBFS concrete by qualitatively comparing the autogenous shrinkage and stress evolution, while the influence of creep and autogenous expansion were often neglected. The stress evolution of restrained concrete is a combined result of not only autogenous deformation but also aging creep. Therefore, an in-depth understanding and accurate quantification of EAC requires a unified model to couple autogenous deformation and aging creep. However, the lack of data of early-age autogenous deformation and aging creep also poses difficulties in development of computational models. In view of the limitations mentioned above, this study establishes a modelling framework based on Rate-type creep law and Bayesian Optimization for quantifying stress evolution of restrained GGBFS concrete. Two TSTM tests were firstly carried out on GGBFS concrete of different w/b ratios. Then, with a self-defined material constitutive subroutine, the creep/ relaxation behavior was implemented as a 13-units Kelvin chain in 3D FEM modelling based on the Rate-type creep law. By forward modelling, the proposed model was validated. By inverse modelling based on Bayesian Optimization, the effects of aging creep on EAC were quantified under the framework of Euro code and ACI code.

2. Experimental

2.1. Materials and mixtures

Two mixes of GGBFS concrete with different w/b ratios were studied. The GGBFS concrete was made from CEM III/B 42.5, with 25% of OPC and 75% of GGBFS. The detailed mixture proportions are shown in Table 1. The chemical composition of utilized CEM III/B 42.5 is listed in Table 2. The composition was measured with a PANalytical AXIOSmAX Advanced 4 kW Rh 60 kV LiF220 Ge111-c PX1 spectrometer on powder pressed pellets. Superplasticizer (MasterGlenium 51) with a water reducing rate of 35% was used in the mixture of w/b = 0.35. The

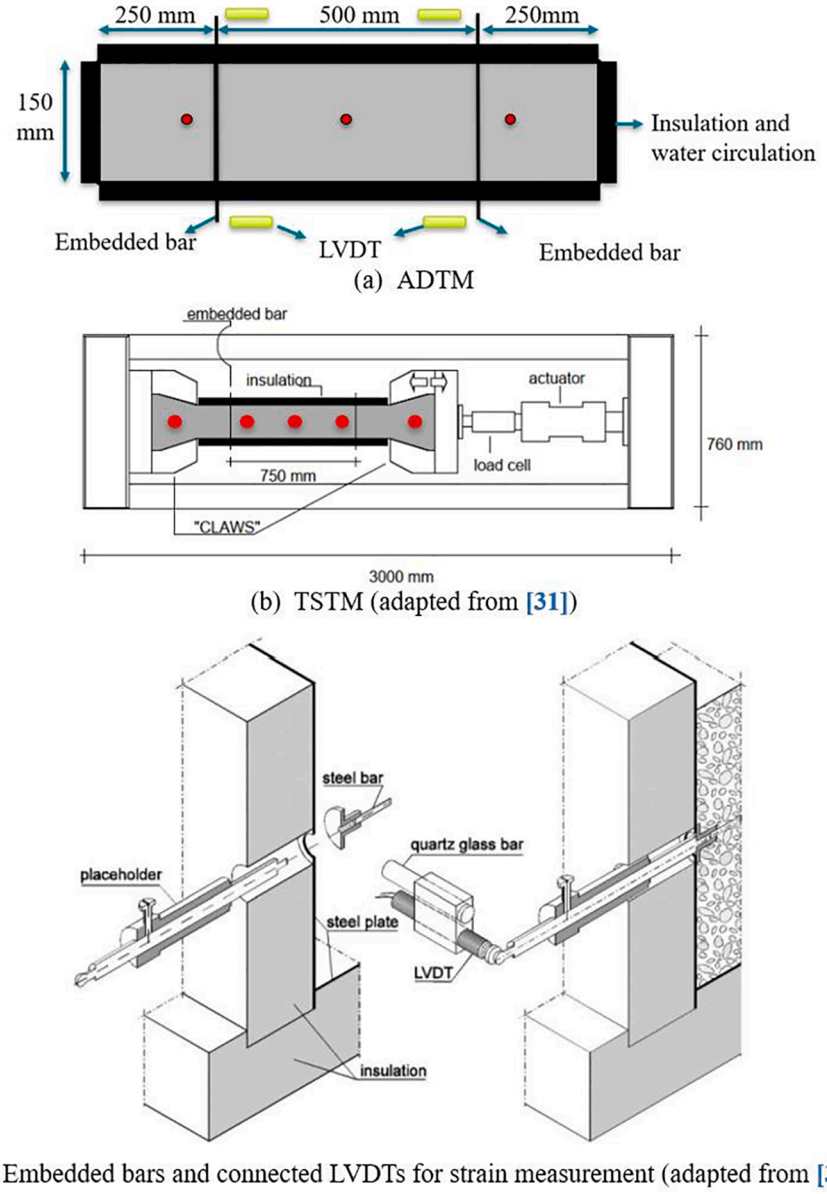

Fig. 2. Test Setup.

compressive strength results of the two mixes, which will be used as inputs for modeling, are shown in Fig. 1. To ensure that all autogenous shrinkage-induced stress is taken into account, the test should start at the timing (i.e., time-zero) when the concrete is hardened enough to generate stress under restraint condition. This study chose the setting time of cement paste measured by Vicat tests as the time-zero [30]. For the mix with w/b = 0.35 and 0.5, the setting time was measured to be 7.5 and 8 h, respectively. The slump testing results of the mix with w/b = 0.35 and 0.5 were 40 mm and 90 mm, respectively. Since the workability of w/b = 0.35 was already suitable for casting and adding too much superplasticizer can introduce high risk of bleeding, the dosage of superplasticizer was not further increased. The test for the mix with w/b = 0.35 lasted 35 days, while the one with w/b = 0.50 lasted 28 days. The reason accounting for longer duration of the mix w/b = 0.35 was that the stress results showed much more fluctuation in 26 ~ 28 days (see Fig. 11b). Therefore, the testing duration for w/b = 0.35 was extended to 35 days to double-check the fluctuations.

2.2. Test setup

The test setup was formed by two major parts: Autogenous Deformation Testing Machine (ADTM) and TSTM, as shown in Fig. 2 [31]. The red dots indicate the positions where thermal couples were installed. The ADTM allowed the sealed specimen to deform freely, so that the autogenous deformation of the middle part can be measured by two embedded bars and connected Linear Variable Differential Transformers (LVDTs), as presented in Fig. 2 (a). The TSTM restrained the relative distance between the two embedded bars to zero and then the stress was measured (see Fig. 2 (b)). Before concrete casting, the embedded steel bars were fixed in the ADTM and TSTM mould by external placeholders (see Fig. 2 (c)). When the concrete specimen reached its setting time, the placeholders were removed and calibrated LVDTs were attached to the embedded bars to measure the strain.

To exclude thermal deformation and effects of temperature on autogenous deformation, the temperature of the concrete during the test was controlled at 20 degrees by circulating temperature-regulated water around the TSTM and ADTM specimen. The water temperature was adjusted in real time during the test to achieve a pre-specified

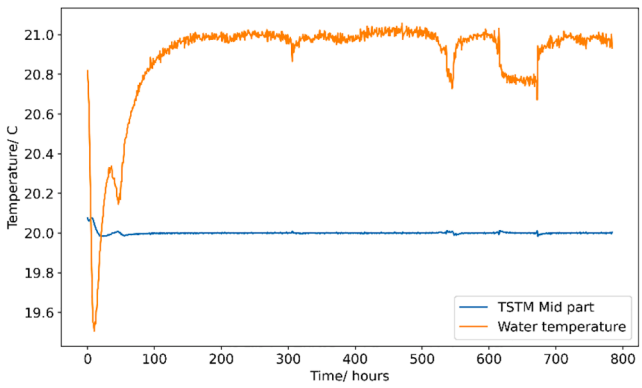

Fig. 3. Temperature history of the TSTM test (w/b = 0.35).

temperature profile based on the temperature measured by embedded thermal couples. To show the effects of temperature control, the TSTM temperature history is given in Fig. 3 as an example. The environmental temperature was kept at 19.2 degrees. To maintain the specimen at a constant temperature of 20 degrees, the circulating water was cooled at first hours to make up for the heat release of hydration reaction and then heated after the hydration peak to compensate for the cooling due to lower environmental temperature.

3. Modelling

The stress evolution is the direct index to measure the EAC potential of concrete. The EAC potential $p(t)$ can be derived by normalizing the stress evolvement history $\sigma(t)$ with the tensile strength $f(t)$ as follows:

$$p(t) = \frac{\sigma(t)}{f(t)} \tag{1}$$

Therefore, the ultimate objective of the modelling work is to predict the stress evolvement history $\sigma(t)$ of GGBFS concrete under fully-constrained TSTM tests. In section 3.1, the basic computational principals and dilemma is illustrated. Then, in section 3.2, to address the computational dilemma, the Rate-type Creep Law is introduced and incorporated in FEM model by a self-defined material subroutine. In section 3.3, the overall governing constitutive equation, autogenous deformation, material properties and boundaries conditions are defined according to testing conditions and results. In section 3.4, the creep compliance function $J(t, t')$ is parameterized under the framework of ACI and Euro codes, and fitted with a 13-units Kelvin chain spectrum. In section 3.5, forward modelling is conducted by using the recommended aging creep formulars of the codes. In section 3.6, based on Bayesian Optimization, inverse modelling is conducted to efficiently find the correct aging creep formular.

3.1. Stress superposition

The build-up of stress under restrained condition is a time-dependent process. Since EAC analysis mainly refers to undamaged concrete, this study assumes that the previous status of concrete does not influence the mechanical response of concrete at later stages. In other words, the mechanical responses of concrete in different times steps are independent from each other. Therefore, the Boltzmann superposition can be applied to sum all mechanical responses of concrete at all time steps to form an overall mechanical response. In TSTM tests, the relative distance of two embedded bars is constrained, which corresponds to typical relaxation scenarios. Therefore, the stress development history $\sigma(t)$ should be expressed as following convolution:

$$\sigma(t) = \int_0^t R(t,t')d\varepsilon(t') \tag{2}$$

where t is the age of concrete; t' is the age when loads are applied; ε is the imposed strain (in this study, ε refers autogenous deformation); R is the relaxation function. To compute the stress superposition in TSTM tests, first divide the whole continuous process of autogenous deformation by a time interval Δt. Suppose in each time interval Δt, the autogenous deformation happens immediately at the onset of the time interval and is kept constant until the end of the time interval (as shown in Fig. 4 (a)). With a fully-constrained boundary condition, at the onset of each time interval, the autogenous deformation (i.e., imposed strain) is

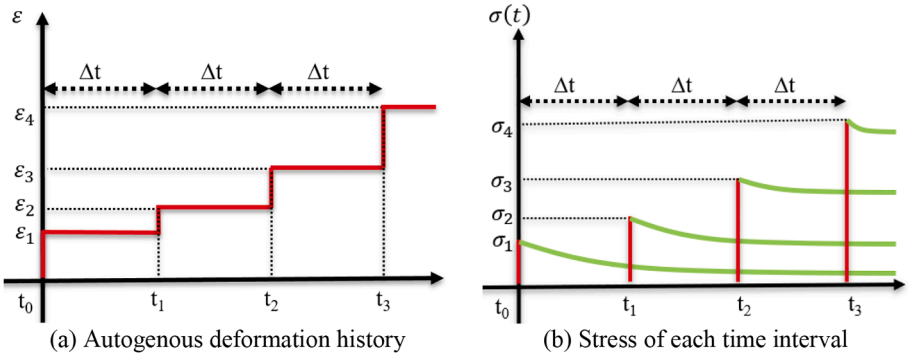

Fig. 4. Illustration of stress superposition.

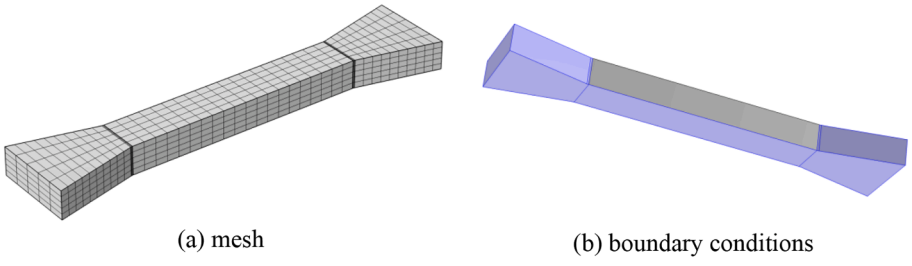

Fig. 5. Numerical dog-bone specimen.

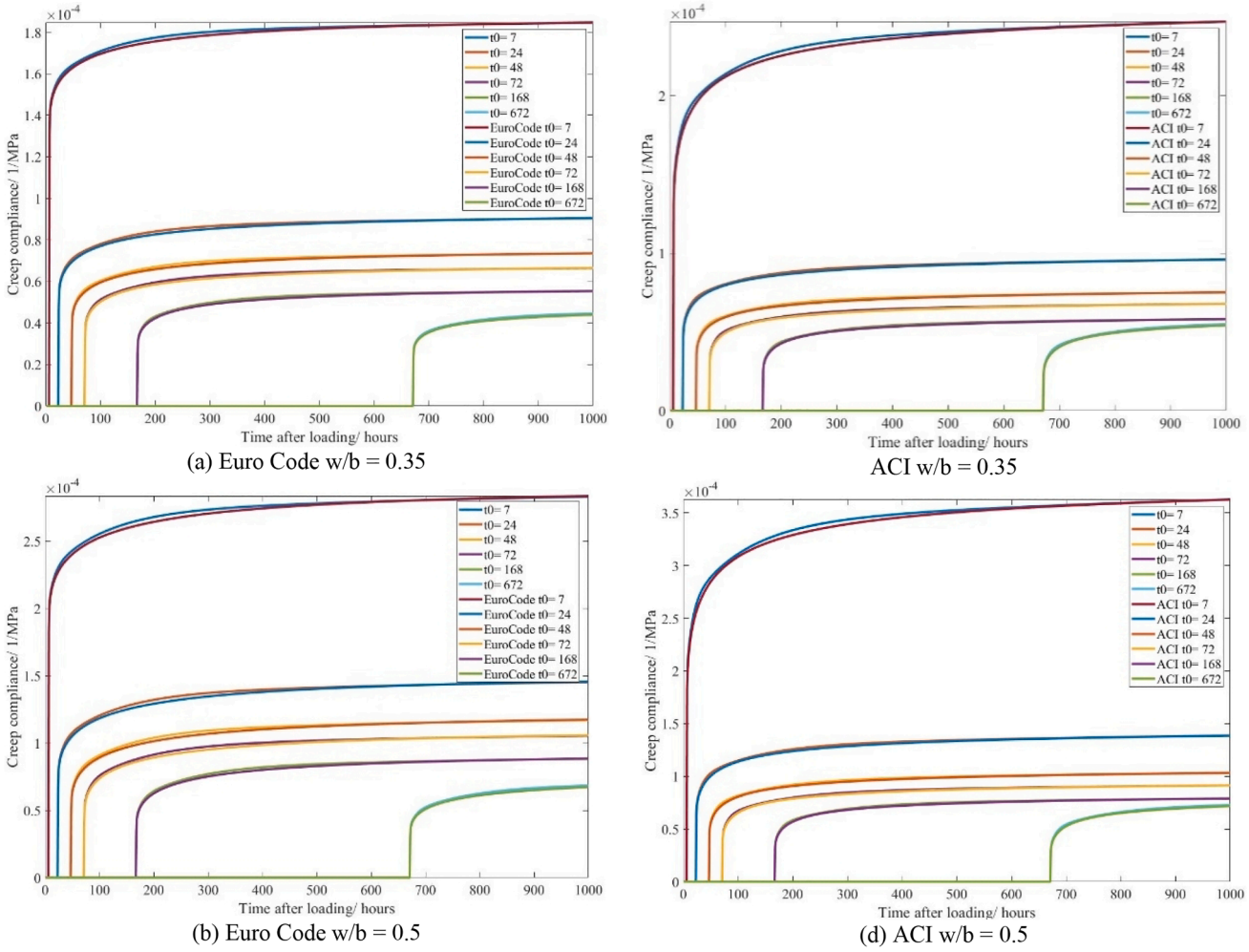

Fig. 6. Fitting results of Kelvin chain with codes (w/b = 0.5).

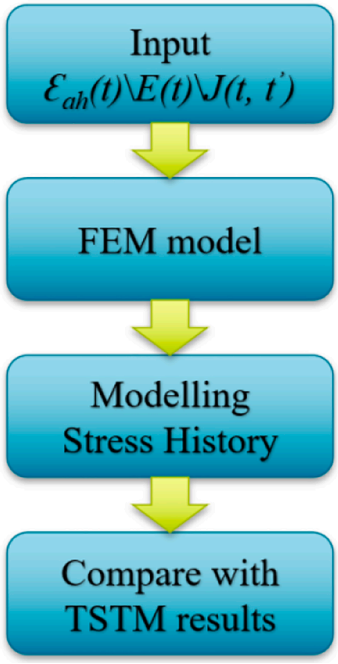

Fig. 7. Workflow of forward modelling.

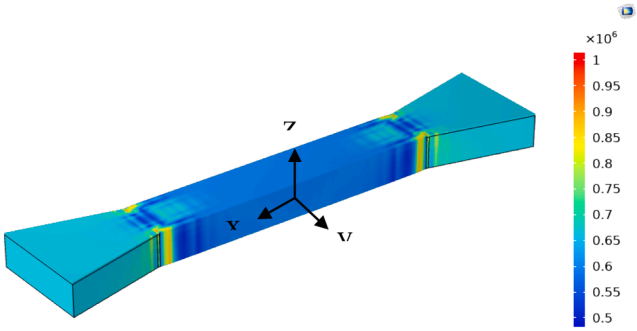

Fig. 8. Stress contour at time = 640 h (w/b = 0.5).

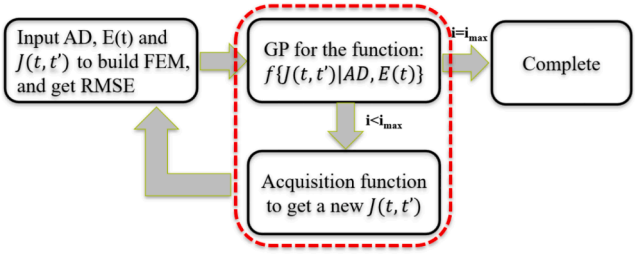

Fig. 9. Workflow of inverse modelling.

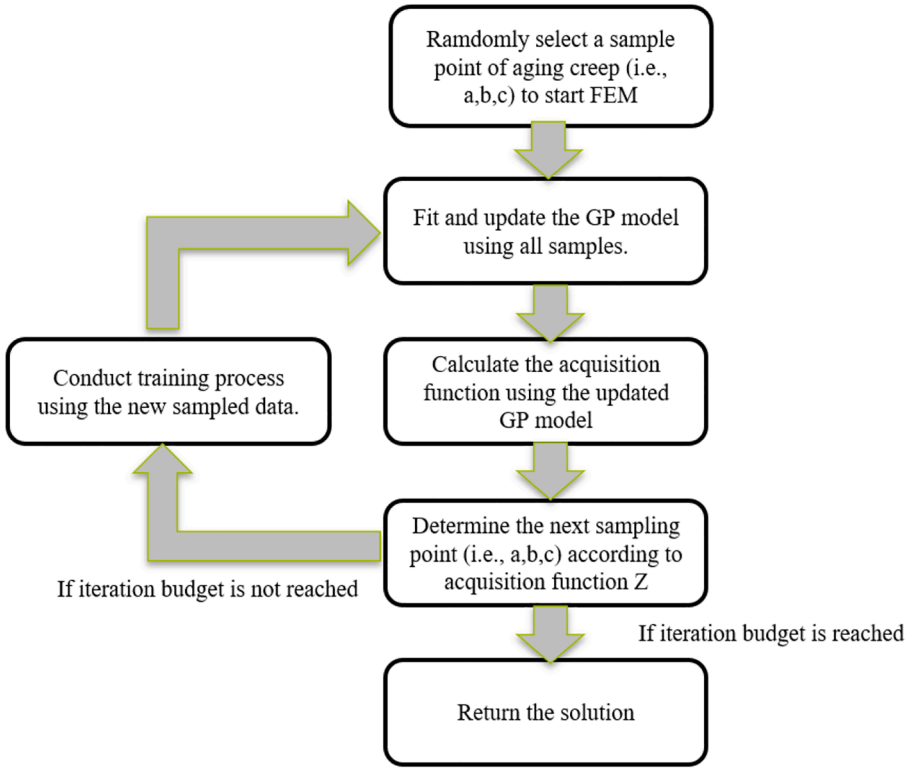

Fig. 10. Workflow of Bayesian Optimization.

constrained and causes stress. Fig. 4 (b) shows the stress history of each time interval corresponding to the strain history of Fig. 4 (a). The red line in Fig. 4 (b) is the instantaneous elastic stress increase induced by imposed strain at the onset of each time interval, while the green line is the relaxation history of the stress.

Followed by Eq (2), the stress evolution after t_3 in Fig. 4 will be the sum of all the stress curves (i.e., green curves), which will be expressed as:

$$\sigma(t) = \varepsilon_1 R(t,t_0) + \varepsilon_2 R(t,t_1) + \varepsilon_3 R(t,t_2) + \varepsilon_4 R(t,t_3) \quad (3)$$

The case showed by Fig. 4 illustrates the computational dilemma of Eq (2), which requires to restore every stress history curve of each previous time interval and sum them up. In the simple examples given in Fig. 4, which only has 4 timesteps, 4 terms of stress histories are needed to count the whole stress evolution history. For realistic applications, where large number of timesteps are needed, direct implementation of Eq (2) in FEM is very difficult because storing all the stress histories of every element will easily cause "out of memory" and result in very low computational efficiency.

3.2. Rate-type creep law

The Rate-type creep law can efficiently solve the computational dilemma introduced in the section [32,33]. The relaxation function *R (t, t')* are difficult to measure due to the fact that the strain must be adjusted to a constant value in a very small time-interval. Therefore, it is more practical to characterize the viscoelasticity from the perspective of creep, which is easier to be tested. The integration form of strain is expressed as:

$$\varepsilon(t) = \int_0^t J(t,t')d\sigma(t') \quad (4)$$

where J is the creep compliance function. Rearrange the Eq (4) into the incremental form from t_i to t_{i+1} and assume a linear stress variation in each time interval, one can get the quasi-elastic constitutive equation:

$$\Delta\sigma = E^*\Delta\varepsilon - \sigma^* \quad (5a)$$

$$E^* = \frac{\Delta t}{\int_{t_i}^{t_{i+1}} J(t_{i+1},t')dt'} \quad (5b)$$

$$\sigma^* = E^*\int_0^{t_i}[J(t_{i+1},t') - J(t_i,t')]\dot{\sigma}dt' \quad (5c)$$

where $\Delta\sigma$ and $\Delta\varepsilon$ are difference of stress and strain between two consecutive time steps t_i and t_{i+1}. Note that the integration in Eq (5c) still requires to revisit all load history, which makes FEM modelling very difficult. By implementing the Rate-type Creep Law [32,33], the integral expression can be transformed to a series of linear differential equations, which are the governing equations of the Kelvin chain rheological model with multiple sets of spring and dashpot. The creep compliance function can be firstly expressed as a Dirichlet series:

$$J(t,t') = \frac{1}{E_0(t')} + \sum_{j=1}^{N}\frac{1}{E_j(t')}\left(1 - e^{-\frac{t-t'}{\mu_j}}\right) \quad (6)$$

where N is the number of Kelvin chain units; E_j and μ_j is the elastic modulus and retardation time of j-th Kelvin chain units. Assuming the variation of stress within each time interval is linear, substituting Eq (6) into Eq (5b) and Eq (5c) and calculating the integral by mid-point rule, one can obtain the expression of E^* and σ^* as follows:

$$E^*(t^*) = \frac{1}{\frac{1}{E_0(t^*)} + \sum_{j=1}^{N}\frac{1}{E_j(t^*)}\left(1 - \left(1 - e^{-\frac{\Delta t}{\mu_j}}\right)\frac{\mu_j}{\Delta t}\right)} \quad (7a)$$

$$\sigma^*(t_i) = E^*(t^*)\sum_{j=1}^{N}\left(1 - e^{-\frac{\Delta t}{\mu_j}}\right)\varepsilon_j^*(t_i) \quad (7b)$$

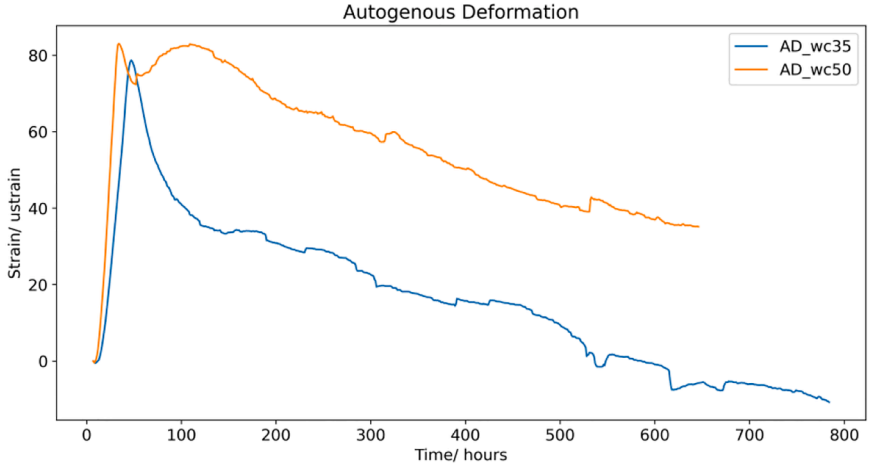

(a) Testing results of autogenous deformation measured by ADTM

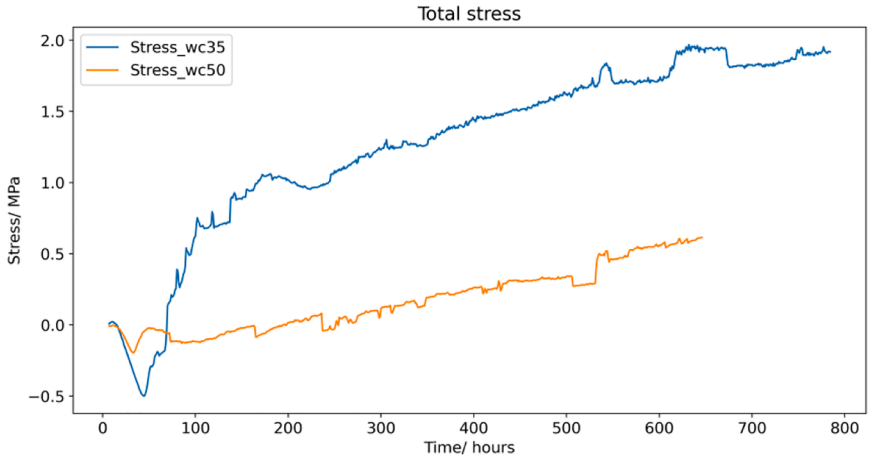

(b) Testing results of stress evolution measured by TSTM

Fig. 11. ADTM and TSTM test results.

$$\varepsilon_j^*(t_i) = \int_0^{t_i} \frac{1}{E_j(t')} e^{-\frac{t_i - t'}{\mu_j}} \dot{\sigma} dt' \tag{7c}$$

$$\varepsilon_j^*(t_{i+1}) = e^{-\frac{\Delta t}{\mu_j}} \varepsilon_j^*(t_i) + \frac{1}{E^*(t_i)} (1 - e^{-\frac{\Delta t}{\mu_j}}) \frac{\mu_j}{\Delta t} \Delta\sigma \tag{7d}$$

where t* is the average of two consecutive time steps t_i and t_{i+1}. Eq (5a) and Eq (7a ~ d) encompass the incremental viscoelastic constitutive relationship for simulating the development of stress induced by autogenous deformation. Note that the ε* of each Kelvin chain unit is the internal state variable, which is a second-order strain tensor that has to be updated on each integration point according to Eq (7d) at every time step.

3.3. FEM configuration

The Rate type creep law is implemented by a self-defined subroutine of material mechanical constitutive behavior in the commercial FEM software COMSOL Multiphysics. A numerical dog-bone TSTM specimen is generated as shown in Fig. 5, which is discretized by evenly-distributed hexahedral mesh. At the transition area from the two ends to the middle, more densified meshing scheme is adopted to assure numerical precision. The FE model uncertainties are significant factors influencing the optimization results. Since the input parameters (except for creep aging terms) are derived from tests, the only variation lies in the FE configurations, including step size, step convergence criterion, meshing schemes, etc. These parameters were calibrated at the very beginning to get reliable results. The influence of different meshing schemes is investigated and the results are given in the Appendix B. Roller boundaries are attached to the highlighted purple area in Fig. 5 (b) (i.e., bottom sides and the lateral sides of the two ends), which ensues zero displacement in the normal direction of the boundary surface.

Considering the autogenous deformation as an isotropic deformation in all direction, then the quasi-elastic constitutive equation described by Eq (5a) becomes as follows:

$$\Delta\sigma = E^*(\Delta\varepsilon - \Delta\varepsilon_{ad}) - \sigma^* \tag{8}$$

where $\Delta\varepsilon_{ad}$ is the autogenous strain happening in each time interval; σ^* is the state variable that stores the previous load histories and should be updated in every time step according to Eq(7a ~ d). In this model, there are three kinds of input material properties and behaviors: autogenous strain $\varepsilon_{ad}(t)$, elastic modulus $E(t)$ and creep compliance function $J(t, t')$. The results of ADTM are directly used as input of autogenous strain $\Delta\varepsilon_{ad}$. The results of compressive strength shown in Fig. 1 is used to calculate the $E(t)$ [34]:

$$E(t) = E_{c0}\partial_E \left(\frac{f(t)}{10}\right)^{\frac{1}{3}} \tag{9}$$

where $f(t)$ and $E(t)$ is the compressive strength and elastic modulus at an age t, respectively; E_{c0} is a coefficient and equals to 21500 MPa; α_E is the

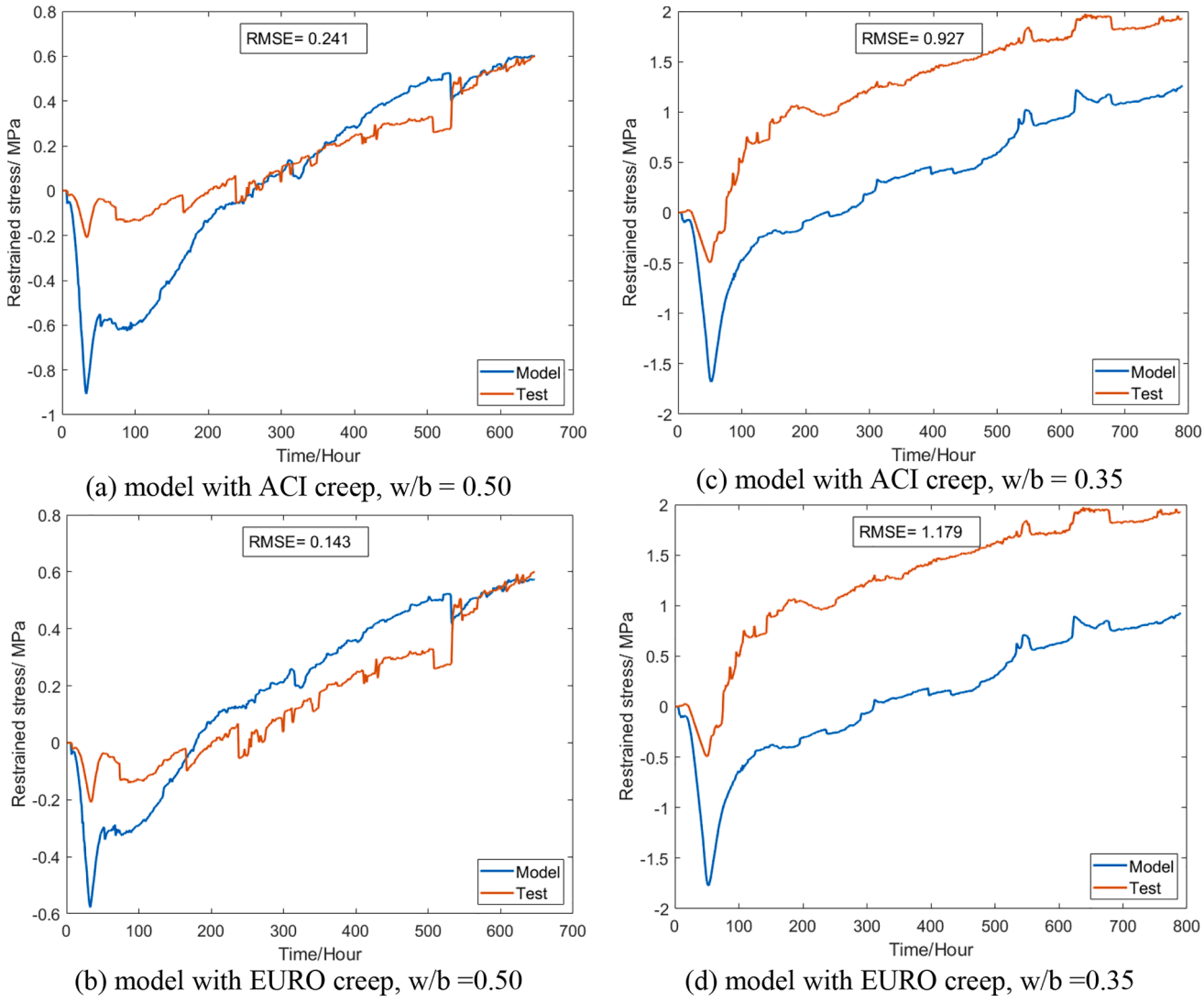

Fig. 12. Simulated stress evolution with different codes for creep compliance.

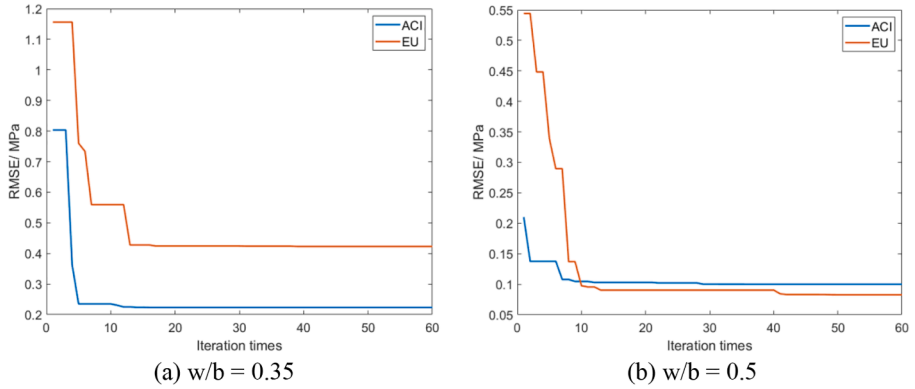

Fig. 13. Optimizing history.

coefficient for different aggregate ranging from 0.7 to 1.2. Considering the aggregates used in the tests are mainly quartzite gravel, α_E equals to 1.0 in this study. Note that the selection of a proper estimation formula for the elastic modulus can influence the modelling results. The influence of 4 international codes [34-37] on the simulation results were investigated, by using their different formulas in the model. The results are shown in Appendix-C.

The bottleneck of this model lies in the creep compliance function $J(t, t')$, which is hard to be tested because 1) the creep tests last certain time range, which makes it difficult to decouple the influence of elastic modulus evolution and shrinkage, especially for very early age concrete; 2) creep tests can only get data of creep compliance function at several

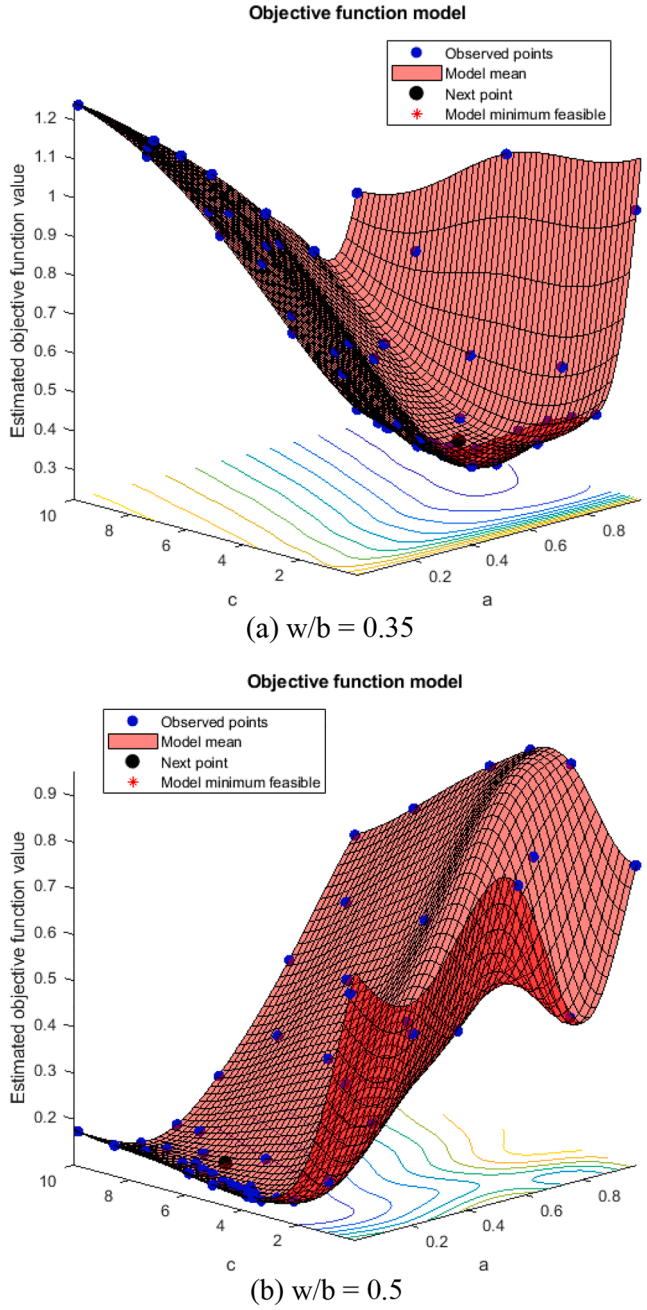

Fig. 14. Objective function for the model with ACI codes.

ages of loading, while *J(t,t')* is a continuous function characterized by a 2D surface.

3.4. Kelvin chain spectrum for creep compliance function

To solve the problems of lacking creep compliance data, this study parameterizes the creep compliance function *J (t, t')* into a continuous Kelvin chain spectrum under the framework of two international standard codes: Euro Code 2 [35] and ACI-209R [36]. Firstly, the *J (t, t')* recommended by the codes is used as input in this model to evaluate the performance of the codes; Then, inverse modelling is efficiently conducted by Bayesian Optimization to find the most appropriate *J (t, t')* of GGBFS concrete. Both these two codes follow the expression of Double Power Law [10], and their formulars can be uniformly expressed as:

$$J(t,t') = \frac{1}{E(t')} + C_0 C_1(t') C_2(\xi) \tag{10}$$

where C_0 is a coefficient related to general concrete properties and environmental conditions, such as compressive strength at 28 days, relative humidity, etc.; C_1 is a power function to describe the aging of creep compliance, which only depends on age of loading t'; C_2 is a power function representing the non-aging term, which mainly depends on the time length of loading ξ ($\xi = t\text{-}t'$). For more detailed calculation of these parameters, one can refer to the codes [35,36].

In the Rate-type law, the creep compliance function is expressed as a Kelvin chain model (i.e., a Dirichlet series as Eq (6)). Therefore, to incorporate the creep compliance data of codes in the FEM model, the Kelvin chain parameters (i.e., E_j, μ_j for j = 1: N) should be firstly fitted by the function Eq (10). However, directly fitting the E_j, μ_j tends to be problematic because of weak points such as non-unique solutions [38]. This study implements a general procedure that fitting the Kelvin chain parameters with a continuous spectrum [39], which guarantees a unique and stable solution.

A 13-units Kelvin chain (j = 13 in Eq (6)) is adopted to describe the creep compliance function Eq (10) in first 28 days. Firstly, the retardation time μ_j is chosen as a priori to prevent ill-conditioned equation system as follows [40]:

$$\mu_j = 10^{-6+j},\ j = 1{:}13 \tag{11}$$

The continuous form of the non-aging term is expressed as follows:

$$C_2(\xi) = \int_0^{\infty} \frac{1}{E_j}\left(1 - e^{-\frac{\xi}{\mu_j}}\right) d(ln\mu_j) \tag{12}$$

Using the Laplace transform and Widder's formula, the solutions of E_j can be derived [39]:

$$\frac{1}{E_j} = -ln10 * \lim_{k\to\infty} \frac{(-k\mu)^k}{(k-1)!} C_2^{(k)}(k\mu) \tag{13}$$

In this study, the spectrum of third order (k = 3) is used. The fitting results of the mixes with w/b = 0.35 and 0.5 are shown in Fig. 6, which shows that the fitted Kelvin chain can mimic the codes with good precision.

3.5. Forward modelling

Forward modelling is the most common modelling approach, as is shown in Fig. 7. With the framework of FEM model established in section 3.1 ~ 3.4, the forward modelling simply goes by inputting the material parameters and get the simulated results of stress development of TSTM tests. In TSTM tests, the stress is calculated by normalizing the restraint force with the area of cross-section of the dog-bone specimen. In the FEM model, as shown in Fig. 8, the modelling result of stress evolution σ_M is calculated at the middle section of the specimen and expressed as follows:

$$\sigma_M(t) = \frac{\iint \sigma_{xx} dydz}{A} \tag{14}$$

where σ_{xx} is the component of stress tensor in xx direction (i.e., axial direction of dog-bone specimen); A is the cross-section area of the yz plane at × = 0. The metric Root Mean Squared Error (RMSE) is adopted to quantify the modelling accuracy by averaging the residual error at each time step:

$$RMSE = \sqrt{\frac{\sum_t (\sigma_M(t) - \sigma_T(t))^2}{t_{total}}} \tag{15}$$

where $\sigma_M(t)$ and $\sigma_T(t)$ is modelling and testing results of stress at time step t.

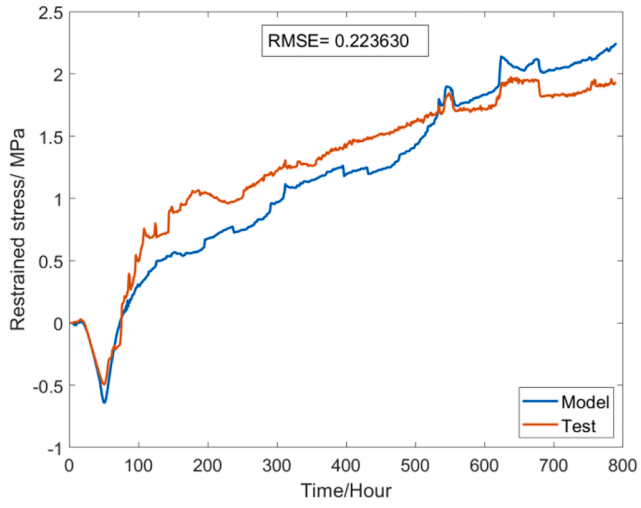

(a) ACI, w/b =0.35

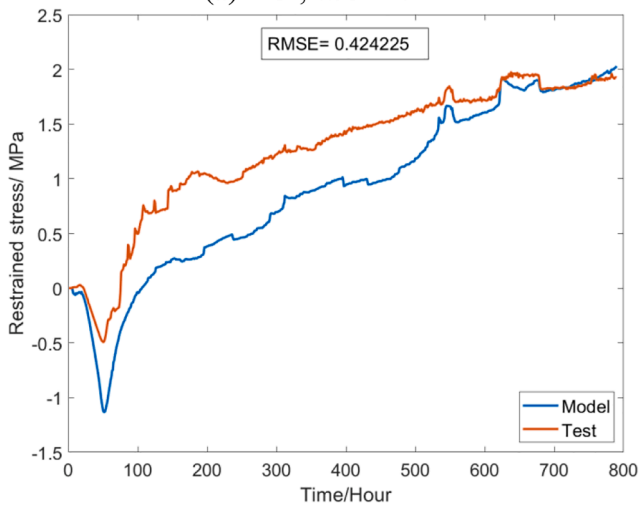

(b) Euro code, w/b =0.35

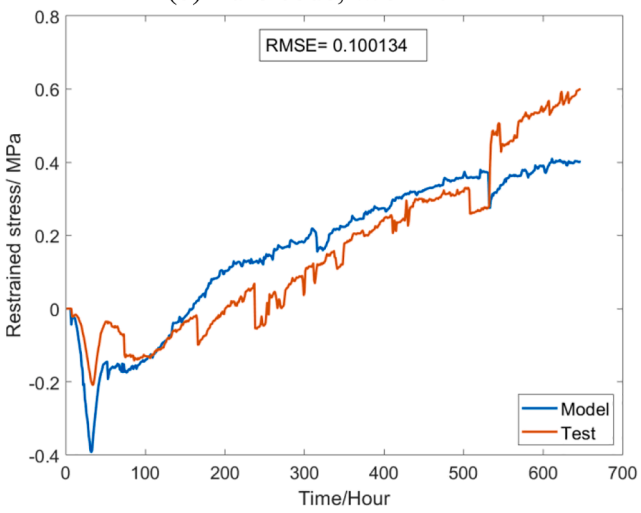

(c) ACI, w/b = 0.50

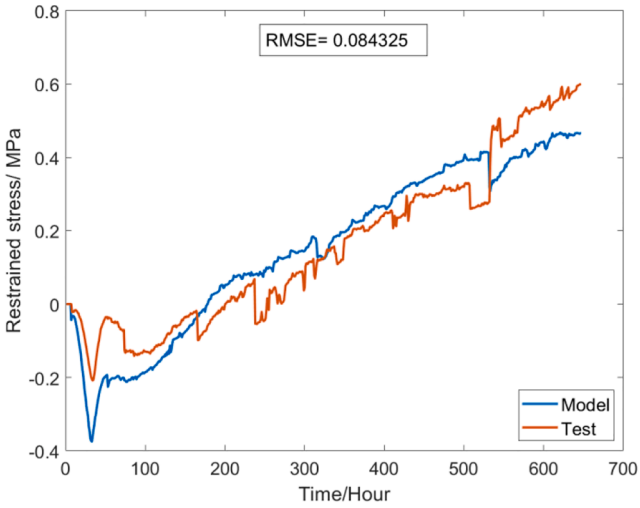

(d) Euro code, w/b = 0.50

Fig. 15. modelling results with adjusted aging term of creep.

3.6. *Inverse modelling*

Creep tests of concrete at early age are much more difficult to perform because the influence of hydration cannot be fully excluded. For example, for a concrete specimen under sustaining loads from an age of 12 h to 36 h, the measured creep compliance curve from $J(12,12)$ to $J(36,12)$ is expected to be derived by subtracting the shrinkage strains from the measured total strains. Then with the experimental results, the

Table 3
Adjusted aging terms for creep compliance function of GGBFS concrete.

	ACI code ($C_1(t') = \frac{c}{t'^a}$)		Euro code ($C_1(t') = \frac{c}{b+t'^a}$)		
	a	c	a	b	c
Original values	0.118	1.250	0.200	0.100	1.000
w/b = 0.35	0.990	7.786	0.984	0.024	2.373
w/b = 0.50	0.139	5.228	0.903	1.020	9.940

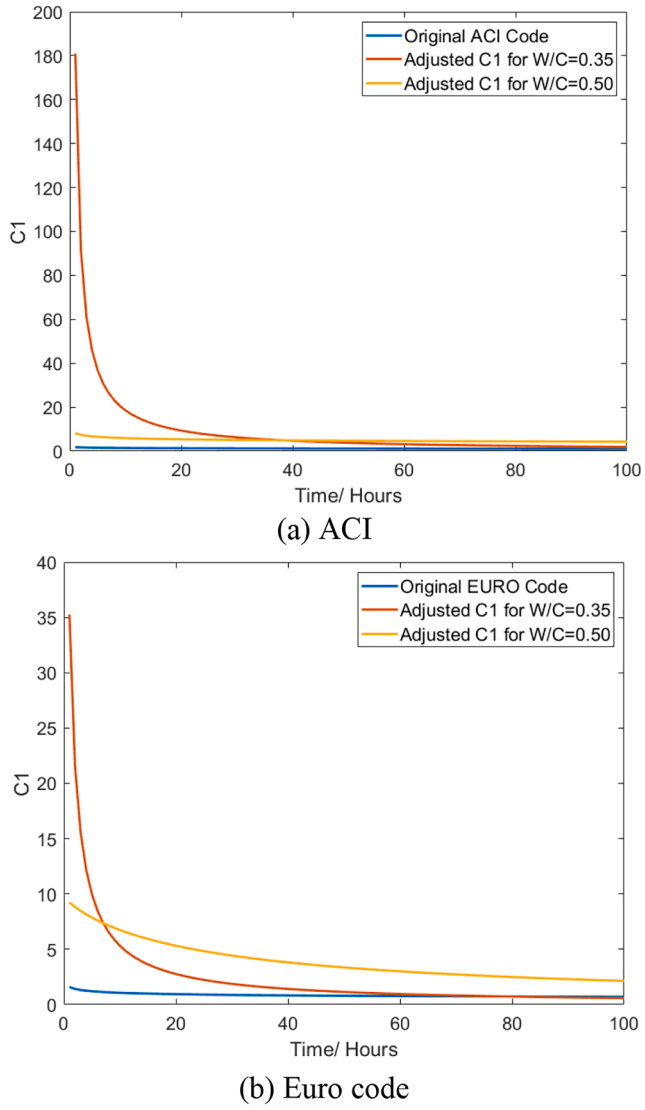

Fig. 16. Adjusted aging term of creep compliance function.

creep compliance function *J (t,12)* will be fitted by either power function or logarithmic function, which aims to represent the strain development since the age of 12 h when a unit load is applied. However, this process assumes the concrete properties (e.g., elastic modulus, creep etc.) remains constant, while in fact from 12 to 36 h the microstructure of concrete changes drastically, which makes the above assumption very untenable. In view of the testing difficulties of aging creep, this study explores the aging patterns of creep by inverse modelling [41-43]. An objective function is firstly defined to measure the agreement between modelling and experimental results. Then Bayesian Optimization is implemented to find the best-fit parameters of aging creep to achieve a minimum in the objective function.

3.6.1. Definition of objective function and process

In forward modelling, a black-box function defined by the FEM model can be expressed as follows:

$$RMSE = f[\varepsilon_{ad}(t), E(t), J(t,t'), \sigma_T(t)] \tag{16}$$

where f is a complex implicit function represented by the FEM model. With the function f, inverse modelling can be defined as an optimization process: Given the input of autogenous deformation $\varepsilon_{ad}(t)$, elastic modulus $E(t)$ and testing results $\sigma_T(t)$, find the best creep compliance function $J(t, t')$ that can give best modelling results. Thus, the objective function of inverse modelling can be expressed as:

$$\text{argmin} f\{J(t,t')|\varepsilon_{ad}(t), E(t), \sigma_T(t)\} \tag{17}$$

As in Eq(10), the creep compliance function $J(t, t')$ is a surface controlled by $E(t)$, constant term C_0, aging term C_1 and non-aging term C_2. As discussed in the section 3.4, the aging term C_1 remains unchanged for different concrete mixes and environmental conditions, which is apparently an arbitrary assumption and can cause significant errors [44,45]. Therefore, the optimization process focuses on the aging term C_1. The aging term C_1 of both codes is firstly generalized as a power function controlled by coefficients a, b, and c:

$$\text{Eurocode}: C_1(t') = \frac{c}{b+t'^a}; \tag{18a}$$

$$\text{ACIcode}: C_1(t') = \frac{c}{t'^a} \tag{18b}$$

Then the inverse modelling process can be further described as:

$$\text{argmin} f\{C_1(t', a, b, c)|\varepsilon_{ad}(t), E(t), \sigma_T(t), C_0, C_2(t-t')\} \tag{19}$$

Note that the function f is non-differentiable and computationally-expensive, since calculating the function f means running the FEM model to get the stress result of the whole time-range. Therefore, an efficient optimization algorithm is needed. This study adopts the Bayesian Optimization to solve this problem, which mainly includes Gaussian Process (GP) [46] and a well-defined acquisition function. The workflow of this process is shown in Fig. 9.

3.6.2. Bayesian Optimization

Solving Eq (19) is a computationally-expansive work because 1) running FEM model is computationally-expansive and 2) high dimensionality of parameters produces large sample space. By fitting the objective function with a probabilistic model, Bayesian Optimization is a smart sampling and efficient global optimization algorithm for expansive black-box function [47,48]. The workflow of Bayesian Optimization in this study is shown as Fig. 10.

By assuming the objective function in section 3.6.1 follows the multivariate Gaussian distribution, the objective function can be fitted by Gaussian Process (GP). For i-th sampling point of aging creep $X_i = (a_i, b_i, c_i)$, the implementation of GP is mainly by fitting the kernel of the covariance matrix as follows:

$$K = \begin{bmatrix} k(X_1,X_1) & \cdots & k(X_1,X_n) \\ \vdots & \ddots & \vdots \\ k(X_n,X_1) & \cdots & k(X_n,X_n) \end{bmatrix} + \sigma_{noise}^2 \boldsymbol{I} \tag{20}$$

in which k is the covariance kernel calculated by an exponential function of the second norm of the difference value between two samples [49]; n is the number of sample points of aging creep that are incorporated in the GP model; σ_{noise} is the standard deviation of the noise, which follows standard normal distribution. Denote the multivariate Gaussian distribution of n sample points of aging creep as $D_{1:n} = (X_{1:n}, Y_{1:n})$, and then the performance (i.e., RMSE of FEM) of next sample point (i.e., (n + 1)-th sample point) can be predicted by Bayesian rules for multivariate Gaussian distribution as follows [46]:

$$Y_{n+1}|\mathrm{D}_{1:n}\ \mathrm{N}\left(\mu(\mathrm{X}_{n+1}), \sigma^2(\mathrm{X}_{n+1}) + \sigma_{noise}^2\right) \tag{21a}$$

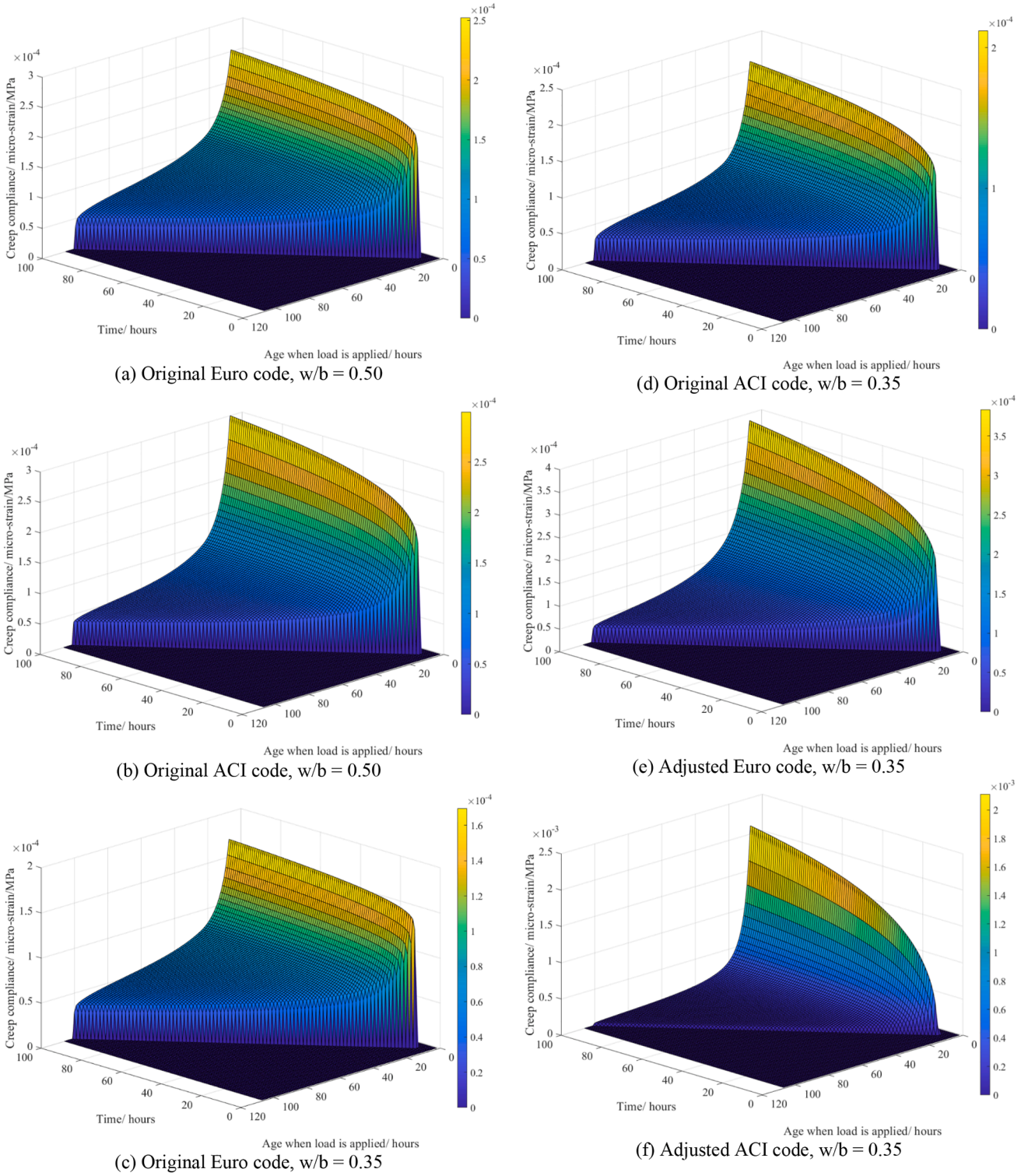

Fig. 17. Original and adjusted creep compliance function.

in which

$$\mu(X_{n+1}) = \boldsymbol{k}^T K^{-1} Y_{1:n} \tag{21b}$$

$$\sigma^2(X_{n+1}) = k(X_{n+1}, X_{n+1}) - \boldsymbol{k}^T (K + \sigma^2_{noise}\boldsymbol{I})^{-1}\boldsymbol{k} \tag{21c}$$

$$\boldsymbol{k} = [k(X_{n+1}, X_1)k(X_{n+1}, X_2)\cdots k(X_{n+1}, X_n)] \tag{21d}$$

Based on GP, the inference of performance (i.e., RMSE of FEM) of any possible sample points can be drawn. Then, the acquisition function (i.e., Expect Improvement [50]) is calculated to infer the improving potential of every possible sample point, as expressed below:

$$I(X_n) = (y_{best} - \mu(X_n))\Phi\left(\frac{y_{best} - \mu(X_n)}{\sigma(X_n)}\right) + \sigma(X_n)\phi\left(\frac{y_{best} - \mu(X_n)}{\sigma(X_n)}\right) \tag{22}$$

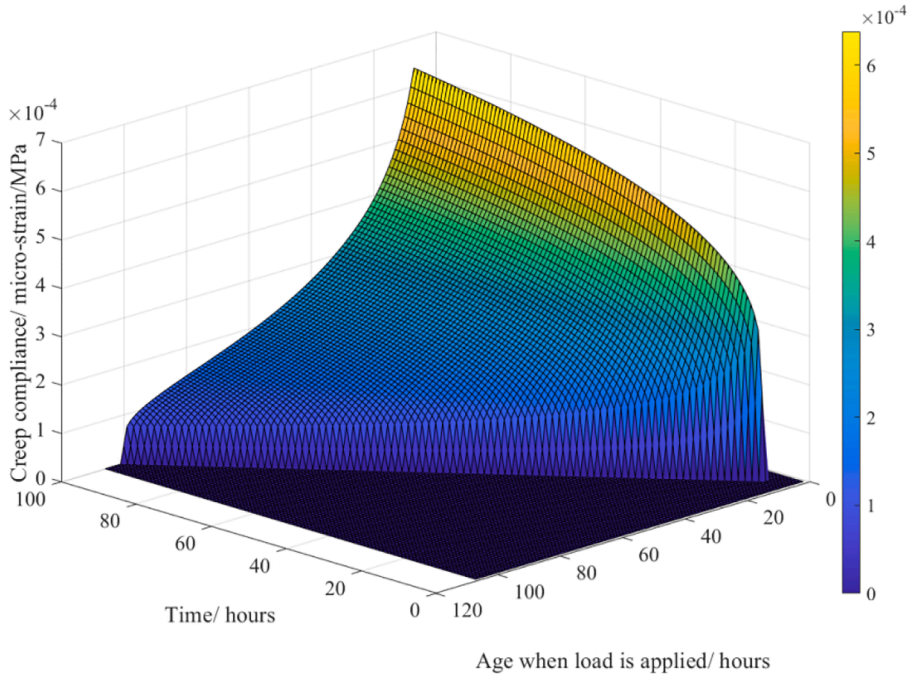

(g) Adjusted Euro code, w/b = 0.50

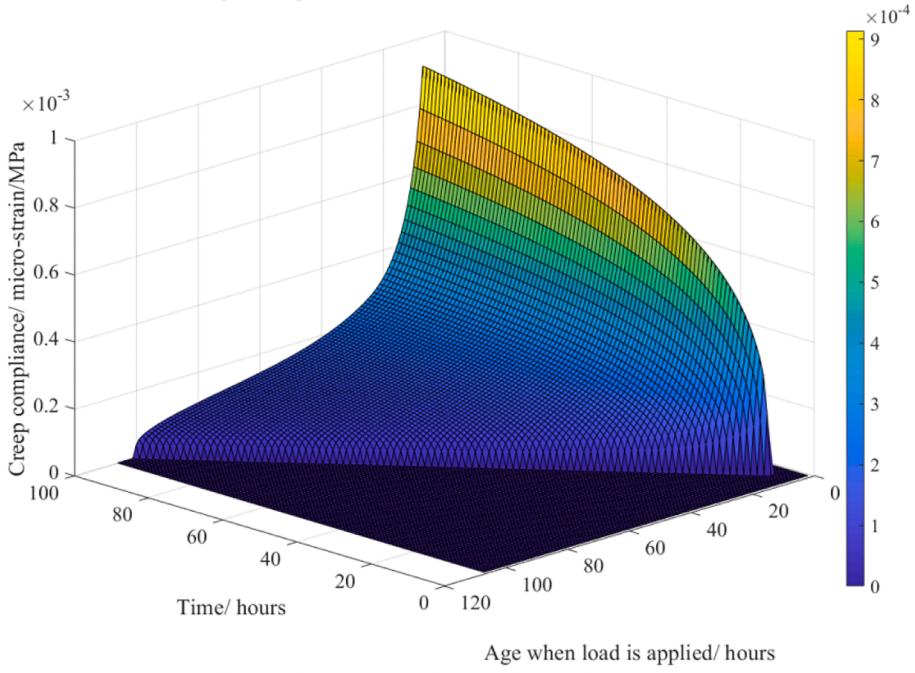

(h) Adjusted ACI code, w/b = 0.50

Fig. 17. (*continued*).

where $\Phi(\cdot)$ and $\phi(\cdot)$ are the standard normal density and distribution function; y_{best} is the tentative optimal value (i.e., lowest RMSE) in current sample space. The first term measures the difference between every possible sample point and the best sample point, which aims to achieve exploitation. The second term assigns more weights to the sample points of more uncertainty to ensure there is no "blank" area in sample space, which achieves exploration. Combining the first and second term, the acquisition function EI tends to get higher values at sample points with lower posterior mean and lower credible intervals, and thus the balance of exploitation and exploration can be achieved.

4. Results and discussion

4.1. Testing results and indications

Results of ADTM and TSTM tests are shown in Fig. 11. From the results of ADTM, high expansion was observed in about first 50 h. Accordingly, the early age expansion caused compressive stress in restraint conditions, as shown in the results of TSTM. The high early-age expansion is due to the fast formation of ettringite, which was clearly observed by Darquennes et al [51]. They conducted DSC test to measure the consumption of the setting regulator by the mineral phases of clinker C_3A and C_4AF to produce ettringite. Their results showed that the

corresponding peak (120 ~ 160 ℃) vanished after 3 days for the CEM III/B sample, which confirmed that expansion phase of slag cement is due to fast formation of ettringite. The magnitude of the expansion of two w/b ratios do not have distinctive difference. The expansion magnitude depends on the producing rate of ettringite and the porosity evolution, which determines the force that expanding ettringite can apply on the pore structures. Because of higher elastic modulus and lower creep, the specimen with lower w/b ratio develops higher compressive stress under restraint conditions. The mix with w/b ratio = 0.5 showed a second autogenous expansion peak, which was attributed to the reabsorption of bleeding water [52]. The second autogenous expansion peak induced corresponding compression stress and significantly delayed the development of tensile stress. In comparison, the mix with lower w/b ratio started shrinking faster in 50 ~ 130 h, which caused drastic increase of restraint tensile stress. This indicates that the period between 50 ~ 130 h has high risk of EAC. The fast shrinkage can be attributed to finer pores and lower internal humidity [53], which can cause high capillary depression according to Laplace and Kelvin laws.

Note that in this study, the ADTM tests started since the setting time. Before the setting time, the autogenous deformation firstly began as fast chemical shrinkage, which was then followed by expansion and shrinkage after setting time. Because the magnitude of stress was very low before setting time, this study did not take the stress result before setting time into consideration. But for different mixes, the stress results may be different. In the future, we will develop a newer version of TSTM and ADTM, which will allow for testing since casting time. The results of autogenous deformation and stress before setting time are shown in the Appendix A. Overall, the testing results of autogenous deformation and stress evolution show the same pattern.

The stress build-up history of GGBFS concrete distinguishes itself with other concrete by a high early age expansion and then a drastic shrinkage, especially for concrete with low w/b ratio. The early-age expansion is clearly in favor of preventing EAC, since it causes compressive stress and delays the development of tensile stress. Especially for GGBFS concrete with high w/b ratios, the reabsorption of bleeding water significantly extends the duration of expansion period and therefore delay the appearance of tensile stress. However, due to the low elastic modulus and high creep/ relaxation of GGBFS concrete, the magnitude of the compressive stress is limited. For GGBFS concrete with low w/b ratios, this poses questions that whether the early-age expansion can survive the GGBFS concrete from the drastic shrinkage in about 50 ~ 130 h after setting time.

Besides, the testing results of TSTM shows limitations in accuracy. Ideally, both the history of autogenous deformation and stress evolution should be a smooth curve. The fluctuation in practical results of TSTM can be attributed to the following 3 possible reasons [54,55]: 1) friction between the specimen and the mold; 2) imbalance of embedded bars at two sides of the specimen; 3) Fluctuation of temperature control system.

4.2. Forward modelling with codes

Fitting the Kelvin chain with ACI and Euro code and inputting the testing results of autogenous deformation and elastic modulus, the modelling results of stress evolution can be obtained, as shown in Fig. 12. By comparing the RMSE, the creep compliance function given by the Euro code produces better results when w/b = 0.50, while the one given by the ACI code prevails when w/b = 0.35. After 200 h, the curves of modelling stress tend to be more parallel with the testing results, which indicates that both codes show good conformity with TSTM testing results at a latter age. However, a very obvious gap at early age shows that both codes do not perform well at an early age. In the results of w/b = 0.35 (see Fig. 12 (c)(d)), although the modelling and testing curves are almost parallel after 100 h, the big difference before 100 h causes significant errors in the whole time-range. If the time-zero of the models and tests are fixed at a time point after 200 h, good conformity between the modelling and testing results can be expected. But in the meantime, this will also cause significant errors since the stress before 200 h is overlooked.

The comparison results of forward modelling suggest that both codes have good performance at a latter age, but when it comes to an early age (e.g., before 200 h), non-negligible errors happen. This defect can indeed be seen from the setup of the creep compliance function in these two codes (see Eq (10)): both codes have specified formulas for calculating C_0 and C_2, depending on different parameters of concrete properties and environmental conditions such as w/b ratios, relative humidity, etc. [35,36]. However, a consistent setting of the aging term C_1 only depends on age of loading t' and remains unchanged for all kinds of concrete under all conditions, as shown below:

$$\text{Eurocode}: C_1(t') = \frac{1}{0.1 + t'^{0.2}}; \tag{23a}$$

$$\text{ACIcode}: C_1(t') = \frac{1.25}{t'^{0.118}} \tag{23b}$$

4.3. Inverse modelling with Bayesian Optimization

Bayesian Optimization can efficiently save the computational resources, as shown in Fig. 13. For the FEM model with ACI code, the minimum is found within 10 iteration steps, while for the model with Euro code, the minimum converges within 15 steps. The reason why the Euro code takes longer than ACI is simply the complexity of aging term: the aging term C_1 in Euro code is controlled by 3 parameters (i.e., a, b, c) while the ACI only have two parameters for C_1 (i.e., a, c).

Since the aging term C_1 of ACI only depends on two parameters a and c, its objective function can be visualized as a 3D surface, as shown in Fig. 14. The distribution of sampling points tends to be much denser when approaching to the minima, and more diluted when approaching to the peaks, which guarantees the tradeoff between exploitation and exploration: 1) more computational resources will be spent to exploit the area that is more likely to have a minimum; 2) certain computational resources will still be allocated to explore areas that have low confidence.

With the inverse modelling, the aging term C_1 of creep compliance function is adjusted to obtain the best modelling results, as shown in Fig. 15. The adjusted parameters for the aging term of creep compliance function $J(t,t')$ is shown as Table 3.

The results with adjusted aging terms show obvious improvement on results with original aging terms of codes. Moreover, it can be found that the major improvement is in early age, since the big gaps before 100 h are effectively reduced. Such changes can also be directly seen from the aging creep term $C_1(t')$ of both codes, as shown in Fig. 16. Note that because ACI and Euro code have different configurations for the constant term C_0 and non-aging term C_2, the magnitudes of C_1 of both codes are different and cannot be directly compared. However, for both codes, the curves of the adjusted aging term C_1 (see Fig. 16) all shows a similar trend: The aging term goes through a fast decrease in first 100 h, and then converges to a certain value that is close to the original aging term given by the codes. Such trend is even more obvious when w/b ratio is 0.35. Overall, the adjusted results prove that much higher creep should be expected for GGBFS concrete at an early age. And creep of concrete with lower w/b ratio goes through a faster aging process, with its early-age creep being much higher compared to the magnitude of creep it will have in a more mature age. The comparison of adjusted creep compliance function with original creep compliance function of the codes are shown in Fig. 17. The 3D surfaces of the creep compliance function still show the same pattern as in Fig. 16~17: a steep slope along the axis "age when load is applied" (i.e., t') is observed, which still indicates that much faster aging of concrete creep at early ages should be characterized to get a more accurate modelling results of stress evolution for EAC analysis.

5. Conclusions

This study presents experiments and numerical modelling of the early-age stress evolution of restrained GGBFS concrete, considering the development of autogenous deformation and creep. Firstly, ADTM and TSTM tests with w/b = 0.35 and 0.5 were carried out to obtain the history of autogenous deformation and stress evolution. Then, by incorporating a self-defined material subroutine based on the Rate-type creep law, the FEM model for simulating the stress development in TSTM tests was established. The creep compliance function was fitted with a 13-units continuous Kelvin chain, which was then inputted in the FEM to characterize the continuous relaxation. Using the creep compliance function proposed by the ACI code and EURO code, this study conducted forward modelling to predict the stress development and evaluate the performance of codes. Finally, this study conducted inverse modelling with Bayesian Optimization to efficiently improve the settings of aging terms in the creep compliance functions of the two codes, and shed light on the aging pattern of creep/ relaxation of GGBFS concrete. The major conclusions are as follows:

(1) The results of ADTM and TSTM tests both indicated that the GGBFS concrete firstly go through high autogenous expansion and then a drastic autogenous shrinkage, before and after an age of 50 h. Although the expansion-induced compressive stress delays the development of tensile stress, the magnitude of compressive stress is low due to high relaxation and slow modulus development. For GGBFS concrete with low w/b ratios, drastic autogenous shrinkage happening in about 50 ~ 130 h after setting time can induce fast increase of tensile stress and therefore pose high threats of EAC.
(2) Using the 13-units continuous Kelvin chain, the creep compliance function can be fitted with good accuracy and incorporated in FEM modelling by Rate-type Creep law. Using the creep compliance function recommended by the Euro code and ACI code as input, the modelling and testing results showed good conformity after 200 h, which validated the soundness of the proposed FEM model in modelling the stress evolution of restrained GGBFS concrete due to autogenous shrinkage and relaxation.
(3) Due to the arbitrary settings in the aging of creep, both codes did not perform well in prediction of early-age stress development. The big gaps in early-age prediction result in significant errors in the stress calculations in whole time-range.
(4) By Bayesian Optimization, inverse modelling was conducted to efficiently find the aging patterns of creep of GGBFS concrete. The modelling results with the adjusted aging terms shows obvious improvement in the prediction of early-age stress development.
(5) The adjusted aging terms suggested that both Euro code and ACI code significantly underestimate the early-age creep of GGBFS concrete. The results also indicated that GGBFS concrete with lower w/b ratios tend to cause faster aging of creep in first hours.

This research encompasses forward and inverse modelling techniques for EAC analysis, and proves the importance of aging creep/ relaxation in prediction of stress evolvement of restrained concrete. In the future, more reliable testing methods should be developed to directly measure the aging creep to provide parameters for forward modelling of EAC analysis.

Declaration of Competing Interest

The authors declare that they have no known competing financial interests or personal relationships that could have appeared to influence the work reported in this paper.

Acknowledgements

Minfei Liang, Ze Chang and Yidong Gan would like to acknowledge the funding supported by China Scholarship Council under grant number 202007000027, 201806060129 and 201706130140. The authors appreciate Mr. Ton Blom's help in preparing and casting concrete. Dr. Marija Nedeljković's help in testing the chemical compositions of materials is also highly appreciated.

Appendix. -A corrugated tube test results

In this Appendix, the results of autogenous deformation and stress buildup before setting time are presented. The stress buildup in the TSTM test is shown in Fig. A1 below. The results show that the stress before setting time is very low. For w/b = 0.35 and 0.50, the stress buildup before setting time only accounts for about 0.1% and 1% of the stress at 28 days.Fig. A2

Due to the fact that the ADTM in this study can only measure the autogenous deformation after setting time, we tested the autogenous deformation by standard corrugated tube test since casting time [56], as shown in Fig. A1. Note that the corrugated tube tests were performed on the CEM III/B paste with w/b ratios being 0.35 and 0.50. The results show that the paste first goes through very high chemical shrinkage before the setting time, and then the expansion and shrinkage start.

Although the chemical shrinkage before setting time is very high, it only induces very low stress. The magnitude of the stress before setting time are considered of minor influence on the overall stress evolution history and therefore was neglected in this study. However, for other mixes, considerable difference may occur if the results before setting is neglected. Therefore, in our future study, the influence of chemical

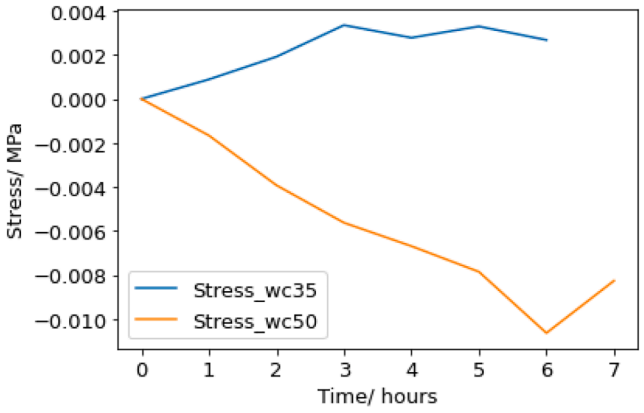

Fig. A1. Results of corrugated tube test for autogenous deformation since casting time.

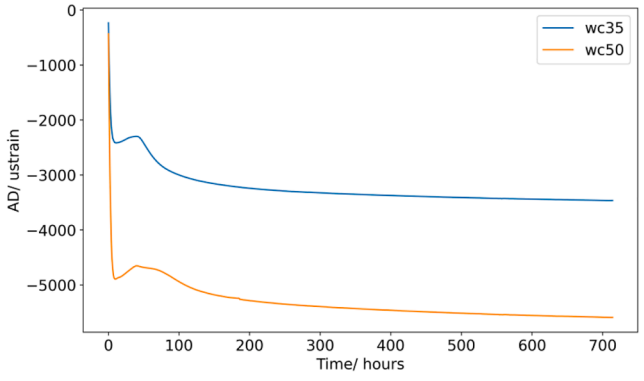

Fig. A2. Results of corrugated tube test for autogenous deformation since casting time.

shrinkage on the stress buildup will tested with a newer version of TSTM setup.

Appendix. -B influence of meshing schemes on the modelling results

In this appendix, influence of meshing sizes on modelling results is shown. Four meshing sizes are given here, including original mesh size, 1 coarser mesh size (166.7% of current mesh size), and 2 finer mesh size (71.4% and 55.6% of original mesh size), as shown in Fig. B1.Fig. B2.

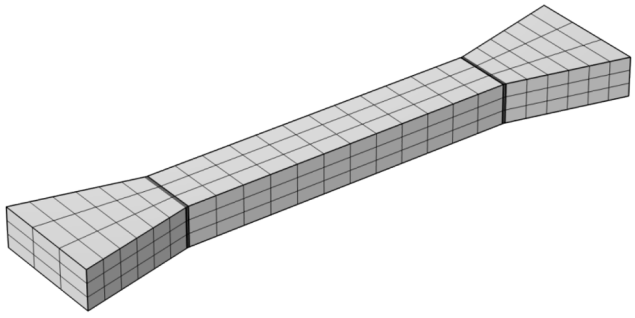

(a) 166.7% original mesh size (element number 270)

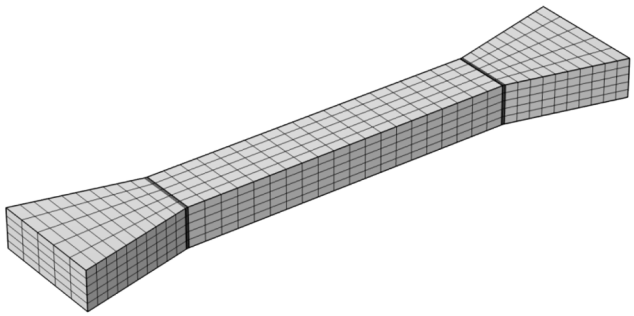

(b) original mesh size (element number 1150)

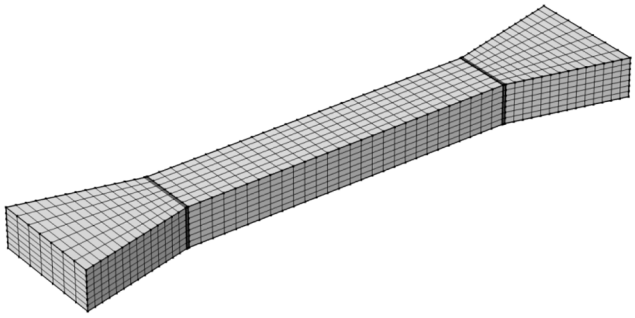

(c) 71.4% original mesh size (element number 3038)

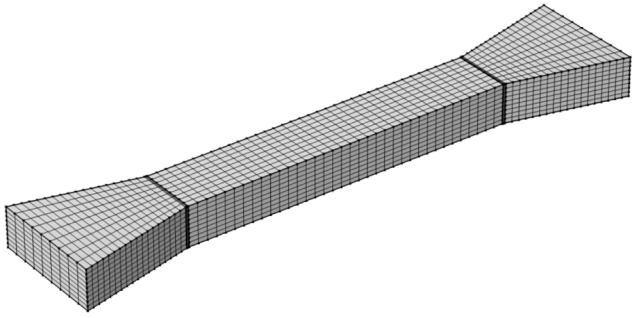

(d) 55.6% original mesh size (element number 6318)

Fig. B1. Four meshing schemes.

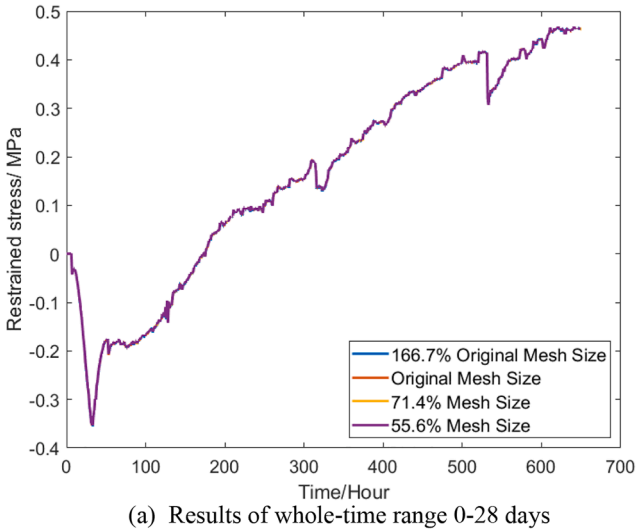

(a) Results of whole-time range 0-28 days

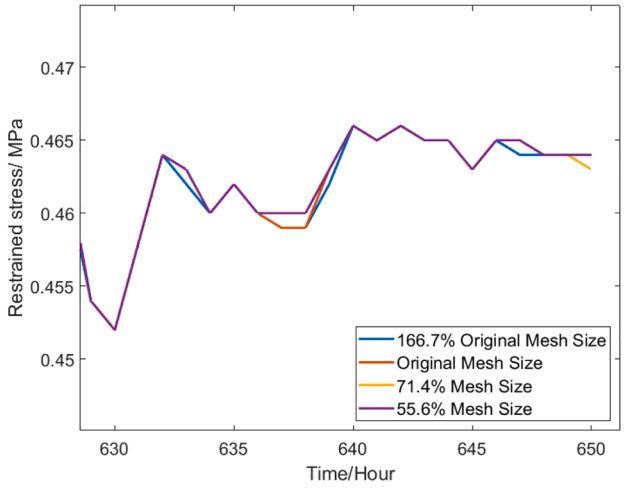

(b) Results between 630-650 hours

Fig. B2. Results of 4 different meshing schemes.

Taking the mix of w/c = 0.50 as an example, the results of the 4 meshing schemes are shown below. It can be found that all 4 meshing schemes can produce similar results. The difference between different meshing schemes remains almost invisible from the whole-time range. Minor difference can only be seen on amplified time range. Therefore, the current FEM configurations can efficiently guarantee the repeatability of the numerical model with the same material input.

Appendix. -C influence of different estimation formulas of elastic modulus

The simulation of w/b = 0.50 was conducted, using the formulas of elastic modulus in 4 international codes [3437]. Based on the compressive strength of the mix w/c = 0.50 at different ages, the elastic modulus can be calculated according to formulas in the 4 international codes, shown as Fig. C1Fig. C2

Furthermore, based on the calculated elastic modulus based on four different international codes, taking the w/b = 0.50 specimen as example, the stress results are shown below. The difference between the codes' estimation on elastic modulus is reflected in the stress results: 1) Because Eurocode 2 and fib MC2010 has similar estimation on elastic modulus, their stress results are also close; 2) Because ACI and CSA tend to underestimate the elastic modulus, their stress results showed lower compressive and tensile stress among the whole-time range. The parametric study we present here also validate the reasonability of our model.

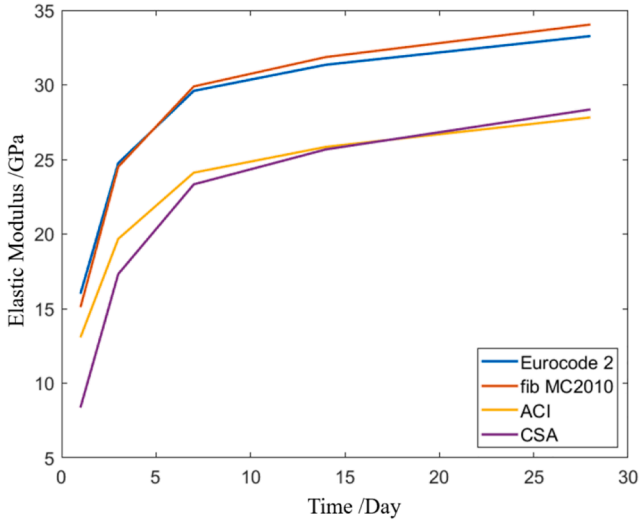

Fig. C1. Elastic modulus of the mix w/b = 0.50 based on 4 international codes.

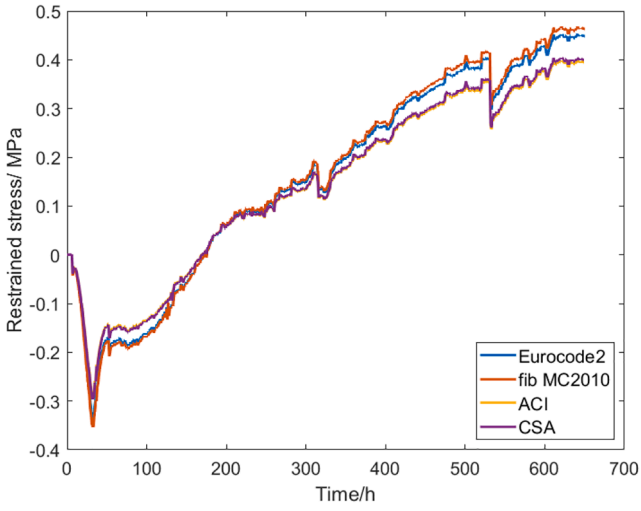

Fig. C2. Stress results of the mix w/b = 0.50 using expressions of elastic modulus of 4 international codes.

References

[1] T. Lu, Z. Li, H. Huang, Effect of supplementary materials on the autogenous shrinkage of cement paste, Materials 13 (15) (2020) 3367, https://doi.org/10.3390/ma13153367.

[2] A. Darquennes, M.I.A. Khokhar, E. Rozière, A. Loukili, F. Grondin, S. Staquet, Early age deformations of concrete with high content of mineral additions, Constr. Build. Mater. 25 (2011) 1836–1847.

[3] P. Lura, O.M. Jensen, J. Weiss, Cracking in cement paste induced by autogenous shrinkage, Mater. Struct. 42 (8) (2009) 1089–1099.

[4] D. Shen, Y. Jiao, Y. Gao, S. Zhu, G. Jiang, Influence of ground granulated blast furnace slag on cracking potential of high performance concrete at early age, Constr. Build. Mater. 241 (2020), 117839.

[5] L. Barcelo, M. Moranville, B. Clavaud, Autogenous shrinkage of concrete: a balance between autogenous swelling and self-desiccation, Cem. Concr. Res. 35 (2005) 177–183.

[6] J. Carette, S. Joseph, Ö. Cizer, S. Staquet, Decoupling the autogenous swelling from the self-desiccation deformation in early age concrete with mineral additions: Micromacro observations and unified modelling, Cem. Concr. Compos. 85 (2018) 122–132.

[7] M. Azenha, F. Kanavaris, D. Schlicke, A. Jędrzejewska, F. Benboudjema, T. Honorio, V. Šmilauer, C. Serra, J. Forth, K. Riding, B. Khadka, C. Sousa, M. Briffaut, L. Lacarrière, E. Koenders, T. Kanstad, A. Klausen, J.-M. Torrenti, E.M. R. Fairbairn, Recommendations of RILEM TC 287-CCS: thermo-chemomechanical modelling of massive concrete structures towards cracking risk assessment, Mater. Struct. 54 (4) (2021), https://doi.org/10.1617/s11527-021-01732-8.

[8] V. Šmilauer, P. Havlásek, T. Gasch, A. Delaplace, D.-M. Bouhjiti, F. Benboudjema, M. Briffaut, F. Kanavaris, M. Azenha, Hygro-mechanical modeling of restrained ring test: COST TU1404 benchmark, Constr. Build. Mater. 229 (2019) 116543, https://doi.org/10.1016/j.conbuildmat.2019.07.269.

[9] Z. Li, S. Zhang, X. Liang, G. Ye, Cracking potential of alkali-activated slag and fly ash concrete subjected to restrained autogenous shrinkage, Cem. Concr. Compos. 114 (2020), 103767.

[10] Z.P. Bažant, E. Osman, Double power law for basic creep of concrete, Mater. Struct. 9 (1) (1976) 3–11.

[11] Z.P. Bažant, L. Panula, Practical prediction of time-dependent deformations of concrete, Mater. Struct. 11 (5) (1978) 307–316.

[12] M. Briffaut, F. Benboudjema, J.-M. Torrenti, G. Nahas, Concrete early age basic creep: Experiments and test of rheological modelling approaches, Constr. Build. Mater. 36 (2012) 373–380.

[13] M. Irfan-ul-Hassan, B. Pichler, R. Reihsner, C.h. Hellmich, Elastic and creep properties of young cement paste, as determined from hourly repeated minute-long quasi-static tests, Cem. Concr. Res. 82 (2016) 36–49.

[14] Y. Gao, J. Zhang, P.o. Han, Determination of stress relaxation parameters of concrete in tension at early-age by ring test, Constr. Build. Mater. 41 (2013) 152–164.

[15] A. Dabarera, L. Li, V. Dao, Experimental evaluation and modelling of early-age basic tensile creep in high-performance concrete, Mater. Struct. 54 (2021) 130.

[16] P. Rossi, J.-L. Tailhan, F. Le Maou, Comparison of concrete creep in tension and in compression: Influence of concrete age at loading and drying conditions, Cem. Concr. Res. 51 (2013) 78–84.

[17] H.u. Zhangli, A. Hilaire, M. Wyrzykowski, P. Lura, K. Scrivener, Visco-elastic behavior of blended cement pastes at early ages, Cem. Concr. Compos. 107 (2020), 103497.

[18] C. Gu, Y. Wang, F. Gao, Y. Yang, T. Ni, J. Liu, X. Lou, J. Chen, Early age tensile creep of high performance concrete containing mineral admixtures: Experiments and modeling, Constr. Build. Mater. 197 (2019) 766–777.

[19] Y. Gan, M. Vandamme, Y.u. Hongzhi Zhang, E.S. Chen, K. van Breugel, B. Šavija, Micro-cantilever testing on the short-term creep behaviour of cement paste at micro-scale, Cem. Concr. Res. 134 (2020), 106105.

[20] Y. Gan, Y.u. Matthieu Vandamme, E.S. Chen, K. van Breugel, B. Savija, Experimental investigation of the short-term creep recovery of hardened cement paste at micrometre length scale, Cem. Concr. Res. 149 (2021), 106562.

[21] K. Kuder, D. Lehman, J. Berman, G. Hannesson, R. Shogren, Mechanical properties of self consolidating concrete blended with high volumes of fly ash and slag, Constr. Build. Mater. 34 (2012) 285–295.

[22] R. Spingenschmid, Prevention of Thermal Cracking in Concrete at Early Ages, E&FN Spon, London, 1998.

[23] V. Semianiuk, V. Tur, M.F. Herrador, M. Paredes G., Early age strains and self-stresses of expansive concrete members under uniaxial restraint conditions, Constr. Build. Mater. 131 (2017) 39–49.

[24] M. Briffaut, F. Benboudjema, L. D'Aloia, Effect of fibres on early age cracking of concrete tunnel lining. Part I: Laboratory ring test, Tunn. Undergr. Space Technol. 59 (2016) 215–220.

[25] D. Shen, J. Jiang, J. Shen, P. Yao, G. Jiang, Influence of curing temperature on autogenous shrinkage and cracking resistance of high-performance concrete at an early age, Constr. Build. Mater. 103 (2016) 67–76.

[26] A. Markandeya, N. Shanahan, D.M. Gunatilake, K.A. Riding, A. Zayed, Influence of slag composition on cracking potential of slag-portland cement concrete, Constr. Build. Mater. 164 (2018) 820–829.

[27] J. Xin, G. Zhang, Y.i. Liu, Z. Wang, Z. Wu, Evaluation of behavior and cracking potential of early-age cementitious systems using uniaxial restraint tests: A review, Constr. Build. Mater. 231 (2020) 117146, https://doi.org/10.1016/j.conbuildmat.2019.117146.

[28] M. Bouasker, N. El Houda, P.M. Khalifa, Nabil Ben Kahla. Early-age deformation and autogenous cracking risk of slag–limestone filler-cement blended binders, Constr. Build. Mater. 55 (2014) 158–167.

[29] A.E. Klausen, T. Kanstad, Ø. Bjøntegaard, Terje Kanstad, Øyvind Bjøntegaard, Adv. Mater. Sci. Eng. 2019 (2019) 1–15.

[30] Pietro Lura, Jon Couch, Ole Mejlhede Jense, Jason Weiss. Early-age acoustic emission measurements in hydrating cement paste: Evidence for cavitation during solidification due to self-desiccation. Cement and Concrete Research 39 (2009) 861–867.

[31] S.J. Lokhorst, Deformational Behaviour of Concrete Influenced by Hydration Related Changes of the Microstructure, Delft University of Technology, 2001.

[32] G. Di Luzio, L. Cedolin, C. Beltrami, Tridimensional long-term finite element analysis of reinforced concrete structures with rate-type creep approach, Appl. Sci. 10 (2020) 4772.

[33] Z.P. Bažant, M. Jirásek, Creep and Hygrothermal Effects in Concrete Structures, Springer, Dordrecht, The Netherlands, 2018.

[34] International Federation for Structural Concrete (fib), Fib Model Code for Concrete Structures 2010, Ernst & Sohn, Wiley, Berlin, Germany, 2013.

[35] EN. EN 1992-1-1 Eurocode 2: Design of Concrete Structures—Part 1-1: General Ruels and Rules for Buildings; CEN: Brussels, Belgium, 2005.

[36] American Concrete Institute Committee 209 (ACI). Guide for Modeling and Calculating Shrinkage and Creep in Hardened Concrete; ACI Rep. 209.2R-08; ACI: Farmington Hills, MI, USA, 2008.

[37] CSA Technical Committee. Reinforced Concrete Design, A23.3-04, Design of Concrete Structures; Canadian Standards Association: Rexdale, ON, Canada, 2004.

[38] Z.P. Bažant, I. Carol, Viscoelasticity with aging caused by solidification of nonaging costituent, J. Eng. Mech. ASCE 119 (1993) 2252–2269.

[39] Z.P. Bažant, Y. Xi, Continuous retardation spectrum for solidification theory of concrete creeps, J. Eng. Mech. ASCE 121 (2) (1995) 281–288.

[40] Z.P. Bažant, Creep and Shrinkage in Concrete Structures; Mathematical Modeling of Creep and Shrinkage of Concrete, John Wiley and Sons, New York, NY, USA, 1982.
[41] A. Tarantola, Inverse Problem Theory, Methods for Data Fitting and Model Parameter Estimation, Elsevier Publisher B.V, New York, USA, 1987.
[42] J. Kajberg, G. Lindkvist, Characterisation of materials subjected to large strains by inverse modelling based on in-plane displacement fields, Int. J. Solids Struct. 41 (13) (2004) 3439–3459.
[43] R. Mahnken, E. Stein, The identification of parameters for visco-plastic models via finite-element methods and gradient methods, Model. Simul. Mater. Sci. Eng. 2 (3A) (1994) 597–616.
[44] B. Delsaute, J.-M. Torrenti, S. Staquet, Modeling basic creep of concrete since setting time, Cem. Concr. Compos. 83 (2017) 239–250.
[45] M. Liang, Z.e. Chang, Z. Wan, Y. Gan, E. Schlangen, B. Savija, Interpretable Ensemble-Machine-Learning models for predicting creep behavior of concrete, Cem. Concr. Compos. 125 (2022), 104295.
[46] C.E. Rasmussen, C. Williams, Gaussian processes for machine learning, MIT Press, Cambridge, MA, 2006.
[47] J. Mockus, V. Tiesis, A. Zilinskas, The application of Bayesian methods for seeking the extremum, Towards Global Optimization 2 (1978) 117–129.
[48] D.R. Jones, A taxonomy of global optimization methods based on response surfaces, J. Global Optim. 21 (4) (2001) 345–383.
[49] Andrew Wilson, Ryan Adams. Gaussian Process Kernels for Pattern Discovery and Extrapolation. Proceedings of the 30th International Conference on Machine Learning, PMLR 28(3):1067-1075, 2013.
[50] D.R. Jones, M. Schonlau, W.J. Welch, Efficient global optimization of expensive black-box functions, J. Global Optim. 13 (1998) 455–492.
[51] A. Darquennes, S. Staquet, M.-P. Delplancke-Ogletree, B. Espion, Effect of autogenous deformation on the cracking risk of slag cement concretes, Cem. Concr. Compos. 33 (2011) 368–379.
[52] Ø. Bjøntegaard, E.J. Sellevold, Interaction between thermal dilation and autogenous deformation in high performance concrete, Mater. Struct. 34 (5) (2001) 266–272.
[53] P. Lura, Autogenous deformation and internal curing of concrete, Delft University of Technology, The Netherlands,, 2003. PhD thesis.
[54] D.H. Nguyen, V.T. Nguyen, P. Lura, V.T.N. Dao, Temperature-stress testing machine – A state-of-the-art design and its unique applications in concrete research, Cem. Concr. Compos. 102 (2019) 28–38.
[55] H.e. Zhu, Q. Li, Y.u. Hu, Self-Developed Testing System for Determining the Temperature Behavior of Concrete, Materials (10) 10 (4) (2017) 419, https://doi.org/10.3390/ma10040419.
[56] O. Mejlhede Jensen, P. Freiesleben Hansen, Hansen, A dilatometer for measuring autogenous deformation in hardening portland cement paste, Mater. Struct. 28 (7) (1995) 406–409.